Development of silica-enriched cement-based materials with improved aging resistance for application in high-temperature environments

Development of silica-enriched cement-based materials with improved aging resistance for application in high-temperature environments.

Konrad J. Krakowiak[a,e,†], Jeffrey J. Thomas[b], Simon James[c], Muhannad Abuhaikal[b], Franz.-J. Ulm[e]

[a] *Civil and Environmental Engineering Department, Cullen College of Engineering, University of Houston, Engineering Building 1, Room N-132, 4726 Calhoun Road, Houston, Texas 77204-4003*
† - corresponding author, email: kjkrak@uh.edu

[b] *Schlumberger-Doll Research Center, 1 Hampshire St, Cambridge, MA 02139, USA*

[c] *Schlumberger Riboud Product Center, 1 rue Henri Becquerel, Clamart, 92140, France*

[e] *Civil and Environmental Engineering Department, Massachusetts Institute of Technology, 77 Massachusetts Avenue, Cambridge, MA 02139-4307, USA*

Abstract

Understanding the effects of high temperature (HT) and high pressure (HP) conditions on the microstructure of cement-based materials is critical to the construction and safe operation of deep oil and gas wells. Under such conditions, the persistence of calcium-silicate-hydrate (C-S-H) gel is compromised by ongoing crystallization that, if not controlled, may adversely affect the durability of the cement sheath. This work investigates the effect of silica content greater than 35% by-weight-of-cement (BWOC), silica particle size, and solid volume fraction (SVF) on the microstructure and phase composition of cement-silica blends cured hydrothermally at 200°C and 20.7 MPa. The results of X-ray diffraction and electron microprobe analysis revealed significant impact of these three mix design parameters on the final phase assembly, and on the conversion rate of semi-crystalline C-S-H to gyrolite and 11Å tobermorite. Incorporation of more fine siliceous material suppressed dissolution of coarse silica particles, resulting in a matrix

with improved homogeneity and dominated by fine gel pores. Mixes with lower SVF showed greater formation of 11Å tobermorite, a higher degree of crystallinity and/or greater crystallite size. Prolonged HTHP curing of all systems (up to three months in this study), irrespective of the initial SVF, increased the fraction of capillary pores, indicating void coalesce caused by crystal growth. However, we find that this coarsening is less pronounced in systems with less pore space available for crystallization.

Keywords: Curing (A), Temperature (A), Microstructure (M), Aging (C), Oil-Well Cement (E)

1. INTRODUCTION

In recent years there has been increased interest in oil and gas production from unconventional resources [1]. Shale gas, a natural gas trapped within low permeability shale formations, and heavy oil, an asphaltic, dense and viscous crude oil, are two examples of fossil fuels whose recovery has become technologically feasible and economically sound [2]. However, recovering these energy reserves often requires overcoming hostile downhole conditions, such as high-temperatures (HT) and pressures (HP). The HTHP environment amplifies the risks that exist in conventional wells. Therefore, a higher demand is placed on the reliability of the materials and technologies employed in the well production system.

A vital part of the well system is the cement sheath. Its role is to support the casing and to provide the zonal insolation during well operation and even beyond the well's productive life. When subjected to harsh HTHP downhole conditions, the cement must be capable of resisting a variety of potentially damaging mechanical and physicochemical processes such as mineralogical transformations, excessive crystal growth, thermal stresses or pressure changes. Long-term stability of the cement sheath in HTHP conditions is of critical importance for well safety and maintenance.

It has long been known that the addition of silica to Portland cement, such that the overall Ca/Si molar ratio is decreased to about 1, avoids the early strength retrogression experienced by neat cement slurries cured at temperature above about 100ºC [2, 3, 4]. However, the long term durability and structural performance of silica-enriched cement is still an issue that may compromise the operation of the entire well system leading to failure. In recently published work [5, 6], we identified a 'coarsening mechanism' that negatively affects the microstructure and long-term performance of conventional oil-well cement systems containing 35% silica flour

(ground quartz) by weight of cement (BWOC), and subjected to HTHP hydrothermal conditions. This microstructure coarsening consists of changes in the nanometer-level microstructure of the cement sheath; specifically, an increase in the size of the fundamental particles (comprised of crystalline CSH, e.g. xonotlite) of the binding matrix as the cement sheath ages (Figure 1a). As a consequence, the pore space undergoes pore coalescence such that fine gel pores are replaced by medium and large capillary pores (Figure 1b), causing a reduction of the specific surface area (SSA). These microstructural changes cause a gradual decline in the compressive strength and fracture toughness of the cement sheath material [5].

In this work we investigated the effects of adding silica in amounts greater than the commonly accepted and used value of 35% BWOC. This includes analysis of phase evolution and composition with X-ray powder diffraction (XRD) and electron microprobe (EPMA) techniques. Additionally, small angle neutron scattering (SANS), mercury intrusion porosimetry (MIP), and electron microscopy (SEM) were used to study the effects of silica particle size and the solid volume fraction of the mix design on the nanotexture evolution during prolonged HTHP treatment.

2. MATERIALS AND METHODS

2.1 Materials Synthesis

All samples were prepared using Class G portland cement (Dyckerhoff, Wiesbaden, Germany). All of the silica used was crystalline α-quartz. Two distinct silica particle sizes were used (see Figure 2). For the D-type specimens, fine and coarse silica powders developed for commercial oilwell cementing, with median particle size $d_{50}\approx 2\mu m$ and $d_{50}\approx 110\mu m$ respectively, were used.

For the T-type specimens, a technical grade silica (MIN-U-SIL®5, US-Silica) with a particle size slightly finer than the fine silica was used.

The mix designs for all specimens are given in Table 1. Systems D1 and D2 contain both fine and coarse silica, and thus have a bimodal distribution of silica particles. While D1 and D2 systems have the same total silica content of 65% by volume of the blend, system D2 contains more fine silica (and thus less coarse silica). The overall Ca/Si molar ratio of the D-system is 0.38, which is low enough to ensure that the silica is never completely consumed. Slurries were prepared at w/c ratio 0.61, cast into cylindrical molds, and pre-cured for one week at room temperature. After that, smaller cores (φ=2.5cm, h=5cm) were extracted from the original samples and subjected to hydrothermal treatment at 200°C and 20.7 MPa. D-system slurries also include a silicone antifoam agent, a polynaphthalene sulphonate dispersant, and a polymer-based anti-settling agent. The total mass of these additives accounts for less than 1.5% BWOC.

The T-system samples contain only fine silica (MIN-U-SIL®5) in the amount of 42% by volume of blend. This corresponds to a total Ca/Si molar ratio equal to 0.83, reflecting the composition of stoichiometric 11Å tobermorite [7], as well as the composition of the D2 specimens with the coarse silica excluded. This set of samples was designed to test the effect of initial packing of the solid material in the cement slurry (which is directly linked to the free volume available for crystallization in the hydrated cement paste) on the extent of C-S-H crystallization, the degree of crystallinity of tobermorite, and the micro-texture of hydrothermally cured cement systems. Therefore, T-system samples were synthesized with three different SVF values (see Table 1), while keeping unchanged the system chemistry, silica particle size, and processing conditions. Cement slurry was prepared with distilled water, cast into PVC molds, and pre-cured in lime solution for 11 days at 25°C. Prior to the HTHP processing, pre-cured samples were cleaned with

fine grit sandpaper to remove any precipitates caused by direct contact with the lime solution. All samples were exposed to hydrothermal treatment from 1 to 7 days at 200°C and 20.7 MPa, and then cooled slowly to room temperature overnight.

2.2 X-ray Powder Diffraction

Representative samples for x-ray powder diffraction were extracted at the mid-height of each specimen. Circular discs covering the entire cross-section of the original specimen, and approximately 1mm thick, were submerged in isopropyl alcohol for 2 hours to remove free water from the paste and stop hydration [8]. The fluid exchange was followed by manual wet grinding in alcohol using an agate mortar. Powdered samples were dried and stored under vacuum until testing. The final step included gentle re-grinding and sample homogenization just before the powder was loaded into the sample holder of the diffractometer. All powder diffraction patterns were collected with a PANalytical X'Pert PRO XRPD multipurpose diffractometer configured in Bragg-Brentano geometry, with a high-speed, high-resolution X'Celerator position sensitive detector, and a Cu – anode source (Cu K-alpha λ=1.541Å). Scans were carried out from 5 to 70° /2θ, with a step size of 0.009° and a speed of 0.5 sec./step. Experimental x-ray patterns were analyzed in HighScore Plus® (PANalytical) package and compared to Powder Diffraction Files (PDF) from the database published by the International Centre for Diffraction Data (ICDD).

Peak profile analysis was run on diffraction data obtained from all T-system specimens (Table 1). Diffraction peaks are modeled as a linear mixture of Gaussian and Lorentzian components with pseudo Voigt function [9, 10] and zero peak asymmetry. The diffraction background was fitted manually with regularly spaced base points. Fits were considered good when the goodness

of fit (GOF) parameter, χ^2, was below 4 and the weighted residual difference, R_{wp}, was below 10% [10, 11].

The instrument contribution to peak broadening was separated from the sample contribution by running an external standard (NIST reference material SRM 660b [12]) under similar analytical conditions and optics as the specimens. The instrument calibration curve was obtained by fitting the standard peak widths with a Cagliotti function [9, 10].

2.3 Small Angle Neutron Scattering (SANS)

2.3.1 Sample preparation and SANS measurement

For SANS analysis, thin coupons were cut using a water-lubricated saw with a diamond blade. These coupons were then manually ground to a uniform thickness of 0.6 mm using 300 grit grinding paper and water as the lubricant. This thickness is small enough to avoid multiple scattering effects in cement-based materials for the Q-range used here. Samples were stored and measured in the water-saturated state.

The neutron scattering experiment was conducted at the National Center for Neutron Research in Gaithersburg, Maryland using the 30-m SANS instrument on beamline NG7. Samples were measured at three sample-detector distances in order to cover the full Q-range accessible by the instrument. For the neutron wavelength of 0.8 nm that was used, this Q-range is about 0.01 – 2 nm-1, associated with scattering from features sizes of about 100 – 1 nm (smaller features generate scattering at higher Q).

The incoherent flat background scattering from these samples was substantial due to the large hydrogen content. This background was determined from Porod fits and subtracted from the

absolute-calibrated SANS data. The Porod fits were also used to determine the SANS surface area for each of the sample according to [13]:

$$S_{SANS} = \frac{C_P}{2\pi\Delta\rho^2}$$

where C_p is Porod constant and $\Delta\rho^2$ is the scattering contrast which has previously been determined for various C-S-H compositions [14, 15, 16].

2.4 Chemical Analysis via X-ray Spectrometry

A quantitative analysis of the chemical composition was carried out with the JEOL JXA-8200 Superprobe electron probe micro-analyzer (EPMA). The polished specimens were analyzed at accelerating voltage 15 keV, beam current 10 nA, beam diameter 1 μm and 10 sec counting time per element with background correction applied at each spot. The raw data were corrected for matrix effects with the CITZAF package [17, 18, 19]. The following minerals were used for standard measurements: synthetic diopside-jadeite for {Si,Ca,Al,Mg,Na}, hematite for {Fe,O}, synthetic orthoclase for {K}, rutile for {Ti} and NiS compound for {S}. The statistical treatment of the microprobe data was carried out with respect to the relative contents of elements, expressed in their atomic fractions (at. %), and applying Finite Mixture Modelling (FMM) [20]. More details may be found in ref. [5].

2.5 Characterization of Material Porosity

2.5.1 Mercury Intrusion Porosimetry and Total Evaporable Water Content

Mercury intrusion porosimetry (MIP) was used to characterize the medium and large capillary porosity, as well as the pore size distribution, of the investigated cement systems, using an AutoPore IV 9500 instrument (Micromeritics, US). The intrusion pressure ranged from 3.5×10^{-3}

MPa to 228 MPa, discretized into 70 pressure steps equally spaced on a logarithmic scale, equilibration time 15 sec., evacuation pressure 50 μm Hg, and mercury filling pressure 3.5×10^{-3} MPa. A value of 140 degrees was assumed for the contact angle, and 0.48 N/m for the surface tension of mercury. Thin disks of cement paste were dried by solvent exchange (isopropanol) followed by oven drying to a constant mass at 50°C. Two samples per specimen were analyzed (with mass of around 0.6 g), and the reproducibility of the measurements was excellent. The bulk density was determined at an intrusion pressure level of 13.8×10^{-3} MPa.

To complete the characterization of the pore domain, the total evaporable water content was determined by vacuum-oven drying of a saturated paste to a constant weight at 105°C. For this test, three samples of each specimen type were measured before and after exposure to hydrothermal conditions.

2.5.2 Classification and Determination of Pore Size Families

The pore size classification proposed by Mindess et al. [21], and previously used in the description of the pore domain evolution of conventional oilwell cement systems [5], is applied in this work. Accordingly, large capillary pores are considered to have sizes in the range 10-0.05 μm, medium capillaries 50-10 nm, and gel pores and interlayer space below 10 nm in size. The relative contribution of each class of pores to the porosity is quantitatively assessed for each specimen by combining the results of MIP and total porosity (TP) calculated from the loss of mass on drying. It is known that drying at 105°C tends to remove the water bound into the internal structure of the C-S-H gel, as well as aluminate phases, resulting in the overestimation of the true porosity associated with free water [22, 23, 24, 25, 26]. However, this measure is used here for relative comparison of specimens subjected to different curing treatments.

3. EXPERIMENTAL RESULTS

3.1 X-ray Diffraction and Qualitative Phase Analysis

3.1.1 Systems D1 and D2

The diffraction spectra obtained for system D1 after curing hydrothermally for different times, together with the qualitative phase assessment, is presented in Figure 3a. All spectra from system D1 show clear reflections originating from the crystalline calcium silicate hydrate (CSH) phase 11Å tobermorite (PDF 45-1480). A distinguishing feature of this phase is the reflection at d≈11.3Å, 2θ≈7.8° corresponding to the distance between adjacent layers [7, 27]. Several other diffraction maxima originating from 11Å tobermorite are apparent, e.g. 2θ ≈16.2°, 2θ ≈28.9°, 2θ ≈30°, and are consistently recorded up to 6 months of hydrothermal curing. The peaks of this phase show significant broadening, suggesting nanometer-scale coherent scattering domains or a structural disorder of the tobermorite crystal structure [27, 28, 29]. Gyrolite (PDF 12-0217) is a second crystalline CSH phase observed in the D1 specimens (see inset to Figure 3a). This phase is identified based on the diffraction line at 2θ ≈4°, corresponding to gyrolite with unit cell dimension c≈22Å [7, 30]. Due to structural similarities, many diffraction lines of gyrolite are convoluted with the tobermorite peaks, and this likely contributes to the observed peak broadening.

Other phases identified in the D1 specimens include α-quartz and calcium carbonate. The latter is clearly evident at the longest curing time and dominates the exterior surface (a crust ≈500μm thick) of the bulk specimen. This observation suggests a carbonation process occurring during HTHP treatment, or during post-treatment sample storage prior to x-ray examination.

Figure 3b shows diffraction spectra obtained for system D2 subjected to hydrothermal treatment from 1 week to 3 months. System D2 contains a greater proportion of fine silica than system D1. The D2 spectra display diffraction maxima with similar 2θ positions to the D1 spectra. As with the D1 system, peaks due to residual α-quartz are evident in all spectra, and calcium carbonate is observed, especially for the longest hydrothermal curing time. However, the number and intensity of diffraction maxima originating from the CSH phases is different for the D1 and D2 systems. For the D2 spectra, the basal reflection of 11Å tobermorite at d≈11.3Å (2θ ≈7.8°) is very weak and just slightly above the background, as compared to much greater net intensity in the D1 spectra. Also, the number of maxima that are clearly attributable to tobermorite phase is lower in the D2 system. A prominent example is the diffraction band at 2θ = 28-33°, where the triplet ≈{28.9; 30; 31.8}°, clearly resolved in the D1 spectra, is replaced in the D2 spectra by two very diffuse peaks centered at d≈0.304nm (29.4°θ), and d≈0.280nm (31.9°θ). Additionally, significant asymmetry of the stronger line is observed. Such features have previously been observed in XRD patterns from poorly crystalline C-S-H phase with Ca/Si ratios similar to that of tobermorite (Ca/Si= 0.83) [28, 31, 32]. On the other hand, theoretical calculations of diffraction patterns from disordered, nanocrystalline (10-20 nm) crystallites of 11Å tobermorite yield similar distribution of maxima and their shapes [29].

3.1.2 System T – phase development

Figure 4 shows X-ray diffraction results for system T specimens with solid volume fractions of 40%, 45% and 50%, cured at 200°C for either 24h (Fig. 4a) or for 1 week (Fig. 4b). All the system T specimens have a global Ca/Si ratio of 0.83, corresponding to the composition of 11Å tobermorite, therefore it is unsurprising that this is the main crystalline product observed in all

specimens after hydrothermal treatment. This tobermorite is accompanied by its precursor C-S-H gel, which is responsible for the diffuse reflections centered at around d≈0.304 nm (29.4°), and d≈0.280 nm (31.9°) [31, 32, 33]. Additionally, a very weak diffraction line at ≈12.6°2θ is unique for xonotlite (PDF 29-0379), a CSH phase that is stable at higher temperatures than tobermorite. However, due to the lack of other significant peaks of this phase it seems to be present in trace amounts.

The crystallization of 11Å tobermorite in system T appears to be strongly affected by the solid volume fraction (SVF). Clear examples of this are seen with the intensities of the (002) basal reflection at ≈11.3Å (2θ=7.80°) (Figure 5a), and of the (220) plane reflection at ≈3.08Å (2θ=28.96°) (insets of Figures 4a and b, Figure 5b). The relative change in the net intensity of the (002) peak, between samples T3 and T1 cured for 24 h, is around 45%, and a similar change is seen after cured for 1 week. Similar intensity reduction is observed for the (220) reflection extracted from the peak profile analysis (appendix, Figure A1). It should be noted that the latter peak may include a minor contribution from the (320) xonotlite reflection located at very similar 2θ angle.

Based on the proportionality I∝X [10, 34], where I is the relative x-ray intensity and X is the weight fraction of a component in the mixture, it can be inferred that lower SVF values, as well as prolonged HTHP curing, lead to increased formation of 11Å tobermorite (Figure 5a,b) at the expense of its precursor C-S-H gel. Taking the intensity of the 3.06 Å C-S-H band as a measure of the amount of this phase, the intensity ratio $R = I_{tob}^{220}/I_{C-S-H}^{3.06\text{Å}}$ can be used as a qualitative indicator of the relative amounts of crystalline CSH phases and poorly crystalline C-S-H. These are the two major expected phases in the hydrothermally cured matrix. As the SVF increases, the intensity ratio *R* decreases, indicating less conversion of C-S-H to tobermorite under the same

curing condition (see Figure 5b). Thus, the conversion of C-S-H to tobermorite is greater in the systems with more pore space available for crystallization.

As shown in Fig. 6, increasing SVF values also result in a slight but measurable decrease in the total matrix concentration of C-S-H and CSH phases, and a corresponding increase in the amount of remaining quartz (see also inset Figure 4a,b). This indicates enhanced quartz dissolution in the specimens with more free space available, with a correspondingly greater amount of matrix formation, confirming the important role of the SVF parameter on the phase development in hydrated cement systems enriched with silica and subjected to HTHP treatment.

3.2 Tobermorite Crystallite Size and Crystalline Disorder vs. SVF

Results of x-ray diffraction combined with the peak profile refinement (appendix, Figure A1) also provide an insight into the crystallinity of calcium silicate hydrates through systematic study of the peak broadening. In general, the major contributors to peak broadening are the crystallite size and micro-strain [10, 35, 36]. The first contribution is described by the Scherrer law [37], which states that the maxima of the diffraction pattern are broadened by an amount inversely proportional to the 'apparent size' of crystallites. The micro-strain contribution refers to deviations from ordered crystal structure such as non-uniform lattice distortions, faulting, and dislocations, which can also cause peak broadening.

The broadening of the (002) basal reflection of tobermorite, quantitatively expressed as the full width at half maximum (FWHM) of the peak, is presented in Figure 5a. The FWHM increases with the SVF for both short and prolonged hydrothermal curing, indicating increased degree of crystallinity and/or greater crystallite size when there is more pore space in the specimen. The crystallite sizes derived from (002) diffraction peak using the Scherrer law for SVF values of

{40%, 45%, 50%} are: {77Å, 70Å, 67Å} for 24h of curing, and {104Å, 83Å, 75Å} for 1 week of curing. These values were calculated assuming the integral breadth as a measure of peak broadening and the Scherrer constant equal to 1. Integral breadth, in contrary to FWHM, provides a physical interpretation of the "apparent size": it is the volume average of the thickness of the crystallites measured in the direction normal to the reflecting plane [38]. The unit cell size of tobermorite in the **c**-direction is $d_{002} \approx 11.3$Å. Therefore, greater crystallite size tends to display higher number of stacked layers, which turns to be controlled by SVF as well as the duration of HTHP curing.

The change of the peak broadening with respect to SVF for the (220) reflection of tobermorite is plotted in Figure 5b. The broadening of this peak follows the same trend previously observed for the (002) basal peak. However, this reflection suffers from a convolution with (320) xonolite line. This fact, combined with the overall uncertainty due to profile refinement of multiple highly overlapping diffraction peaks, makes obtaining a quantitative "size-strain" broadening separation obscure. Nevertheless, the Scherrer equation consistently predicts greater apparent domain size in the **a**-**b** crystal projection, (220) corresponds to 3.08Å spacing between calcium ions in the octahedral layer of tobermorite [39], as compared to crystallite size along **c**-direction.

Finally, it is worth looking at the broadening of C-S-H band centered at ≈3.04Å (see Figure 5b). The FWHM of this very broad reflection appears to be unaffected by the SVF of the T-series specimens, and the same is true of the integral breadth. As a result, the 'apparent size' of the C-S-H crystalline domains obtained from the Scherrer law fluctuates around ≈50Å for all T-samples. Interestingly, features of similar size have consistently been measured as a fundamental elementary block of C-S-H gel present in cement pastes cured under various conditions [14, 40, 41].

3.3 SANS and Nano-Texture of D1 and D2 systems

The effect of curing time on the scattering response of D1 and D2 systems, with different proportions of fine and coarse silica, is presented in Figure 7. The scattering intensity in the D1 system is not greatly affected by the duration of hydrothermal curing considered in this study. The recorded intensities are very close over the entire range of the scattering vector, Q. This observation points toward the size stability of fine nanoscale morphologies of calcium silicate hydrates, developed in the D1 matrix, and exposed to hydrothermal processing up to 6 months. Such stability is also supported by the relatively unchanged values of the specific surface area, SSA, estimated from the Porod's law (Table 2). It is likely that the difference observed between D1(6m) and the two other samples of this group, especially in the lower range of Q, results from experimental variability, rather than structural changes with time.

The nano-texture of the D2 matrix generates significantly more intensity at the highest Q-values, corresponding to a nearly doubled SSA, as compared to the D1 matrix (Figure 7 and Table 2). Additionally, the SSA increases slightly with prolonged HTHP curing. Finally, the approximate start of the high-Q Porod regime, associated with the single-particle scattering $I(Q) \sim Q^{-4}$, shifts to greater Q-values in the D2 specimens (marked with an arrow on Figure 7). Such a shift indicates a smaller size of the nano-scale solid features generating the scattering. In general, both systems show resistance to microstructural coarsening over the investigated time scale.

3.4 Electron Microprobe Analysis and SEM Microscopy

3.4.1 Chemical composition of the matrix

The results of the electron microprobe chemical analysis of the D1 and D2 specimens are presented in the form of calcium-to-silicon (Ca/Si) ratio distributions in Figure 8 and scatter diagrams in multiple projections in Figures 9 and 10.

In general, the two systems display fairly comparable distributions that are only slightly affected by the duration of HTHP treatment. After one week of hydrothermal curing, both D1 and D2 matrices reach the overall mean Ca/Si values close to 0.83, which is the stoichiometric ratio of 11Å tobermorite [7, 27]. This observation is in agreement with the x-ray diffraction examination (see Figure 3a,b). This result is interesting given that the cement slurries of both systems incorporate 65% BVOB of crystalline silica (see Table 1), which results in an overall Ca/Si ratio of the mix equal to 0.38. This ratio would be measured by the microprobe analysis if all of the silica reacted. However, the current results show that the overall gross capacity of the systems to accommodate SiO_4^{4-} into the atomic structure of the CSH matrix is limited to the tobermorite-like stoichiometry. Therefore, a significant fraction of quartz remains unreacted (Figures 3, 9a-b, 10a-b, and 12).

Some of the frequency distributions shown in Figure 8 display a significant tail, with many records falling in the low range of Ca/Si < 0.75. Insight into the origin of this tail is provided by considering the x-ray results (see the inset of Figure 3a) and the statistical deconvolution of electron microprobe data (Table 3, Figures 9 and 10) together. The x-ray analysis for the D1 system clearly shows the characteristic reflections of gyrolite, a low-CaO crystalline CSH with $Ca/Si = 0.66$ [7, 30]. On the other hand, the statistical deconvolution of the microprobe data for

the D1 specimens infers a Gaussian component (#1) with mean Ca/Si equal to μ_1=0.76±0.06 at 1 week (Figure 8a) and μ_1=0.75±0.05 at 3 months (Figure 8b). This component displays significant overlap with the other CSH families in the models corresponding to the optimum fit. It is important to note that the characteristic length scale of the beam-solid interaction volume in the microprobe analysis is ≈1μm [18, 19, 42], which is about four orders of magnitude greater than the x-ray wavelength [36]. Therefore, a large fraction of the observations belonging to the cluster #1 represent actual mixtures of gyrolite and tobermorite phases of minute morphologies present in D1 type matrix. All electron microprobe measurements in this group show minor concentrations of aluminum, iron and sulfur, as well as traces of magnesium (see Table 3).

On the other hand, the Gaussian component #1 describing the low Ca/Si observations in the D2(1w) sample is of a different origin. While some of the the low-Ca/Si records may be linked to gyrolite, which was recorded in the x-ray spectra (see the inset of Figure 3b), many of them result from the presence of both CSH matrix and unreacted fine silica particle in the microprobe interaction volume. This was confirmed by post-measurement SEM inspection of selected electron probe sites clustered in group #1, which revealed the presence of residual quartz in very close proximity. As would be expected, this cluster displays a large standard deviation, which is also due to a small fraction of measurements having a greater abundance of Al and Fe. Finally, the low Ca/Si distribution tail is not present in the D2(3m) specimen (see Figure 8d), indicating almost no contribution of quartz-affected probes to observations of CSH origin.

The mixture modelling applied to D specimens cured for 1 week only reveals two clusters with statistically significant differences in chemical composition: #2A and #3. The first cluster #2A, representing calcium-silicate-hydrates, has the smallest variance among all Gaussian components in the model, as well as low concentrations of Al, Fe and S (see Table 3). The high statistical

homogeneity of this cluster, and near lack of Fe, suggests the possibility of Si-Al substitution within 11Å tobermorite. If so, the substitution seems to be minor as the ratio Al/(Al+Si) ≈ 0.025 is well below the maximum value of 0.14 that can be present in the tobermorite lattice [43, 44, 45, 46] (see Figure 11). For cluster #3, the average concentrations of Al and Fe are much higher, as are those of S and Mg, and the variance on each observable used in the statistical deconvolution is greater as compared to cluster #2. While it is possible that cluster #3 also represents a tobermorite-type phase as is hypothesized for #2A. Considering only $Si^{4+} \rightarrow (Al^{3+},Fe^{3+})$ type substitution, an apparent tail reaching beyond the Al-threshold noted above exists for cluster #3 (Figure 11). Moreover, plotting these data in the Si/Ca vs. (Al+Fe)/Ca projection (see Figures 9e-f and 10e-f), reveals a significant number of observations concentrated along the compositional lines of the garnet-hydrogarnet series [33, 47]. Therefore, we hypothesize that cluster #3 is a mixture of CSH and garnet-hydrogarnet phases. The latter are commonly reported in hydrothermally cured $CaO\text{-}Al_2O_3\text{-}SiO_2\text{-}H_2O$ cement systems [47, 48, 49]. Finally, for samples cured for 3 months, D1(3m) and D2(3m), we infer one more component #2B (Figure 8b-d, Figures 9b,d,f and 10b,d,f) with mean Ca/Si=0.91 and a very homogenous structure. This cluster represents a subgrouping within the CSH family that tends to be established and statistically differentiable only after longer exposure to hydrothermal treatment.

3.4.2 Spatial Variability of HTHP Matrix and Silica Demand

SEM micrographs of D1 and D2 specimens are shown in Figure 12. HTHP treatment of D1 specimens leads to complete consumption of the fine quartz particles, while the coarse particles undergo only partial dissolution. This is demonstrated by the presence of CSH product on the original perimeter of the coarse silica particles, and within existing or newly formed cavities inside the coarse particles. In fact, the amount of fine silica in D1, ≈35% by weight of cement,

can reduce the overall Ca/Si of the matrix to ≈1.2 only (assuming complete hydration of the cement). Therefore, in order to reach the measured value of 0.84±0.11, the coarse silica particles must make a substantial contribution to the pozzolanic reaction.

On the other hand, dissolution of coarse silica was much lower in the D2 specimens. The characteristic rim of CSH was occasionally observed in severely fractured aggregates only. Therefore, in the D2 system the demand for silicon is completely satisfied by dissolution of the fine silica, which is present in the amount ≈60% BWOC. Upon complete reaction of fine quartz the CSH matrix could achieve the overall Ca/Si=0.83, which is slightly below the observed value (Figure 8a, b), hence, there is no requirement for the coarse silica to react. These results clearly show that the finer quartz particles react preferentially on hydrothermal treatment.

3.5 Porosity and Pore Size Distribution Assessed with MIP

3.5.1 Systems D1 and D2 – Fixed SVF, Variable Fine Silica Concentration

Figure 13 shows results of mercury intrusion for systems D1 and D2. It is worth noting that these systems share the same SFV and the total silica amount, but have different amounts of fine silica (15% and 25% BVOB , respectively).

There are substantial differences in the cumulative mercury intrusion curves and derived pore size distributions for the D1 and D2 systems. These differences relate to a) the pore diameter at which the significant mercury penetration first takes place, b) the first and second moments, as well as the modes of the pore size distribution, and c) the fractional contribution of each pore class to the total porosity. The system with the smaller amount of fine silica, D1, displays coarser and more heterogeneous porosity after exposure to HTHP treatment (see Figure 13b). The main penetration of mercury starts at 100 nm pore size for the D1 specimen, which is almost one order

of magnitude greater than what is observed for the D2 specimen (see Figure 13c). Interestingly, the total porosity, bulk density, and skeletal density values are quite comparable between D1 and D2 type specimens (see Table 4).

The initial pore size distribution of the specimens after prehydrating at ambient temperature may be one of the factors responsible for such differences. As can be seen in Figure 13a, a slight shift in the cumulative intrusion curves, as well as pore size distributions, exists between the specimens hydrated for 1 week before exposure to HTHP treatment. This shift could be a result of the initial packing of solid material, which depends not only on the particle size but also on the volume fractions of each type of a particle [50]. On the other hand, a smaller concentration of finer material provides lower specific surface available for pozzolanic reactions, which can affect the kinetics of hydrothermally driven phase transformations, the nature and crystal growth of calcium-silicate phases, and ultimately the microstructure of the cement sheath.

3.5.2 System T – Tobermorite Type Stoichiometry and Variable Solid Volume Fraction

The effect of hydrothermal curing on the pore size characteristics of T-system specimens with tobermorite–type stoichiometry is presented in Figure 14. After prehydration at ambient temperature, all samples demonstrate a cumulative intrusion curve typical of young cement paste [33, 51]. Mercury penetration takes place through wide range of pore diameters encompassing large and medium capillaries, as well as gel pores (Figure 14a). The derived pore size distributions display a strong mode in the domain of large capillaries, 10-0.05 μm [21], which are the remnants of the spaces between the solid particles in the initial slurry. A significant tail at smaller pore diameters is a manifestation of space filling and internal fine porosity of the cement hydration products. In agreement with established trends, an increase in the water-to-binder ratio, w/b, causes a systematic shift in the pore size distribution toward coarser porosity [21, 33, 51].

438 This shift is accompanied by an increase in the total porosity, φ, and a reduction of the bulk
439 density of cement paste, ρ_b, (see Table 5).

440 As expected, the intrusion behavior, and thus the pore structure, changes drastically upon
441 exposure to hydrothermal curing. This effect is presented on Figures 14 (b-c). All HTHP cured
442 specimens show: a) a significant narrowing of the pore size distribution suggesting ongoing pore
443 space homogenization, b) shift of the mode, median and the mean pore size by one order of
444 magnitude toward the gel pores. These effects are clearly illustrated in Figure 14d. As with the
445 pre-cured specimens, the hydrothermally cured pastes display a systematic offset in the intrusion
446 curves depending on the initial SVF of the slurry (Figure 14 b,c). This trend holds regardless the
447 duration of HTHP treatment.

448 Finally, we observe a greater amount of mercury intrusion with prolonged duration of
449 hydrothermal processing, irrespective of the initial value of the SVF. This effect is especially
450 evident for the T2 and T3 specimens (with SVF values of 40% and 45%, respectively) where
451 about 7% increase (absolute) in the cumulative pore volume is recorded at maximum intrusion
452 pressure. This phenomenon is significantly less evident in system T1 with the highest SVF of
453 50%. Interestingly, it is also observed for the mature T2 system prehydrated for over 1 year in
454 ambient saturated conditions followed by HTHP curing (Figure 15). Therefore, this is a general
455 phenomenon associated with a continuous evolution of the microstructure due to HTHP-
456 activated internal processes at the material scale, not dependent on the degree of maturation of
457 the prehydrated cement.

4. DISCUSSION

4.1 Effect of Quartz Particle Size on the Phase Assembly and Micro-Texture

4.1.1 Phase Development

The experimental analysis of the D-type systems, with bimodal size of quartz particles, highlights an important effect of the silica particle size on the phase development in HTHP cured cement. Under conditions of constant SVF and total amount of quartz additive, different partitioning of fine and coarse silica particles resulted in significant changes in the matrix mineralogy. In this respect, the 11Å tobermorite–gyrolite phase assembly emerged upon hydrothermal curing of cement slurry with higher incorporation of coarse quartz (see Figure 3a). On the other hand, greater incorporation of fine silica resulted in the formation of semicrystalline C-S-H product with structural and compositional similarities to 11Å tobermorite. The latter phase assembly was persistent over a time scale of several months at 200°C.

In light of these observed differences, it is useful to consider the possible reaction pathways and process kinetics in order to better understand the hydrothermal formation of calcium silicate hydrates in silica enriched cement systems. As discussed by Greenberg [52], the reaction between silica and calcium hydroxide in solution initiates by chemisorption of silanol groups onto calcium hydroxide surfaces. Silica then reacts with water to form monosilicic acid, $H_4SiO_4(aq)$, which reacts with Ca^{2+} ions and hydroxyl groups to form nuclei of C-S-H that can then grow by continued precipitation. Any of the processes of growth, flocculation, and precipitation of crystals might be rate determining. However, in a dilute system at elevated temperatures the dissolution of silica controls the kinetics of the overall reaction, especially at the very early stages [52, 53, 54, 55, 56]. Since the rate of dissolution of silica, k_d, is proportional

to the available surface area of quartz, $k_d \propto S$, this factor will impact the overall rate of the hydrothermal reaction. While D-type systems are not strictly dilute systems, w/s = 0.24, and the pore solution in the saturated hcp is more complex than in the $CaO - SiO_2 - H_2O$ ternary system [33], the open network of gel and capillary pores exposes silica particles to direct interaction with the aqueous environment. Therefore, the surface available for quartz – water interaction will play an important role in the phase development under HTHP conditions, especially at early stages of the pozzolanic reaction, with measurable consequences on the stable phase assembly. In this regard, the nearly two orders of magnitude size difference between the fine and coarse silica used in the D system (Table 1), results in significantly different specific surface values: 1.13 m^2/g for fine and 0.023 m^2/g for coarse. Taking into account the mix designs, the fine silica provides more than 90% of the reactive surface so, according to the Nernst – Brunner equation [57, 58, 59], the rate at which silica dissolves during early HTHP curing is governed by the amount of fine material, which supplies the majority of $H_4SiO_4(aq)$ to react with Ca^{2+} in the pore solution [31, 33, 60]. Thus, less soluble C-S-H with lower Ca/Si ratio is formed primarily from CH, high-Ca/Si C-S-H gel, and fine SiO_2. In fact, the fine quartz present in the D1 system provides enough SiO_2 to effectively reduce the bulk Ca/Si of C-S-H to ≈1.2 only, with further reduction in Ca/Si requiring consumption of coarse silica. This calculation assumes complete consumption of the CH and such a reaction process is facilitated by uniform spatial distribution of fine C-S-H material within the hcp matrix, which provides local sources of $H_4SiO_4(aq)$, separated by the average distance $\langle l \rangle \ll \langle \mathcal{L} \rangle$ (see Figure 16). Such close proximity of the required reactants, along with the relatively open hcp pore structure established prior to HTHP processing (Figure 13a), effectively reduces the characteristic distance and time for mass transport of

503 species, $t_l \propto \sqrt{l}$, and helps to minimize concentration gradients within the evolving C-S-H
504 matrix.

505 While the coarse material will participate to a minor extent in the initial development of the
506 phase assembly, it is hypothesized that its major role takes place in the later stages if there is
507 significant depletion of the fine silica. This is supported by the presence of a characteristic rim of
508 product around the coarse silica material in the D1 specimens but not the D2 specimens (see
509 Figure 12). According to electron-probe measurements (Figure 8a,b and Table 3), the mean
510 Ca/Si ratio of the CSH matrix in the D1 specimens is 0.84, which is lower than the value of 1.2
511 calculated for complete consumption of the fine silica. Therefore, some dissolution of coarse
512 silica must have occurred. When the coarse particle react, the rate of transport of species will
513 likely be controlled by diffusion through the layer of products building up at the surface. Such a
514 product layer has been widely reported: in autoclaved aerated concrete (AAC) and lime silica
515 bricks [55, 56, 61], in HTHP cured oil-well cement with 35% bwoc of coarse silica addition [5],
516 and in the hydrothermal hydration of single crystals of quartz submerged in CaO-saturated
517 solution [53]. Several studies focused on the reaction kinetics of non-stirred systems containing
518 medium and coarse silica particles in CaO solution revealed a linear scaling between the rates of
519 product formation and silica consumption and the square root of time, indicating diffusion-
520 controlled kinetics [53, 55, 56, 62]. Consequently, it appears that the rate at which the product
521 matrix is supplied with H_4SiO_4(aq) will depend on the combined effects of diffusion of aqueous
522 species through the forming barrier and the growth rate.

523 The mechanism for hydrothermal curing described above for the D1-type system, inferred from
524 *ex-situ* measurements reported in this work, postulates a distinct reaction path for the different
525 size fractions of quartz additive, with each type of process dominating at different stages of

hydrothermal processing. As a consequence, the D1 specimens exhibit a heterogeneous evolution of microstructure. Under this particular combination of slurry design and curing conditions, the composition of the matrix tends to be determined by the free energy of the products (thermodynamic reaction control) rather than by the rate of product formation (kinetic control). This scenario is supported by the x-ray diffraction results (Figure 3a) which display bimodality in the family of crystalline CSH phases, 11Å tobermorite (Ca/Si=0.83) and gyrolite (Ca/Si=0.64). A similar trend is observed in the electron microprobe measurements (Figure 8a,b) and SEM micrographs (Figure 12a), showing a spatially nonuniform matrix composition with two dominant families of low-CaO calcium silicate hydrates. Gyrolite and 11Å tobermorite are equilibrium phases stable up to 200°C before they decompose to truscottite and xonotlite under saturated steam pressure [49, 63]. Application of a higher curing pressure additionally enhances tobermorite stability [64].

Unlike the D1 system, the D2 system contains enough fine silica to lower the matrix Ca/Si ratio to 0.86 without engaging the coarse silica fraction. With rare exceptions of severely fractured particles, a product layer forming at the perimeter of the coarse particles was not observed (Figure 12b). This suggests the suppression of the diffusion step associated with the coarse material and the dominant role of fine silica dissolution. Due to higher concentration of microsilica in the D2 system (70% greater reactive surface area than the D1 system) the reaction rate increases and more dissolved silica can be supplied. This effect has been observed in studies of $CaO - SiO_2$ (quartz) $- H_2O$ systems [54, 65, 66], and is analogous to the hydration of OPC and calcium phosphate cements of different fineness [67, 68]. Likewise, the rate of formation of C-S-H gel via nucleation and growth from the solution increases with the precursor stoichiometry ultimately converging toward Ca/Si = 0.86 as measured with electron microprobe

549 (see Figure 8c-d). Interestingly, this semi-crystalline precursor is persistent in the samples aged
550 for 3 months without displaying signs of conversion to 11Å tobermorite, gyrolite, or xonotlite,
551 all of which have lower free energy [39, 63]. Therefore, it is apparent that the hypothesized
552 increased rate of reaction and the reaction pathway present in D1 type system can be responsible
553 for suppression of C-S-H crystallization and crystal growth, "freezing-in" the matrix in the
554 metastable thermodynamic state, a characteristic attribute of kinetic reaction control [69, 70]. A
555 recent study by Kikuma et al. [66] on hydrothermal synthesis of tobermorite in the $CaO - SiO_2$
556 system, monitored by *in-situ* time-resolved X-ray diffraction at 190°C, reports a similar effect for
557 mixtures incorporating fine quartz (< 2.2 μm) at a water/solids ratio of 1.7.

558 To our knowledge, the current understanding of the crystallization mechanism of C-S-H gel at
559 the molecular level is still unclear. While the importance of the precursor synthesis,
560 stoichiometry and curing conditions on the equilibrium products have been recognized [32, 39,
561 45, 71, 72], the complexity of the underlying processes and the limitations of available
562 experimental methods have prevented a complete understanding of the nucleation and
563 crystallization mechanism in HTHP cement systems. For example, it is unclear whether the
564 mechanism by which C-S-H transforms to tobermorite is topotactic (i.e., internal nucleation with
565 internal order preserved [39, 73, 74]) or through-solution (i.e., dissolution followed by nucleation
566 and growth [32, 72]).

567 One plausible hypothesis for the suppressed conversion of C-S-H to tobermorite in the D2
568 system, which is independent of the specific transformation mechanism, relates to the molecular
569 structure of the C-S-H. As originally proposed by Sato [71], formation of tobermorite seems to
570 be repressed when the C-S-H precursor contains long and/or crossed-linked chains of silica
571 tetrahedral, which is generally case when the C-S-H has Ca/Si ratio < 1 [31]. The transformation

of such a structure to a different crystal structure would be relatively energy intensive, as a greater number of bonds need to be broken as compared to C-S-H with Ca/Si > 1 that contains dimers and short chains. Similarly, less defective C-S-H structures exhibit lower solubility [31, 33, 60] which would limit the rate of nucleation and growth from the solution. For the systems studied here, the initial formation of low-Ca/Si C-S-H in the D2 system could be a consequence of the fast reaction facilitated by the greater availability of H_4SiO_4(aq). Conversely, C-S-H with Ca/Si > 1 is more likely to form initially in the D1 system due to the lower amount of fine silica. Additionally, the diffusion controlled kinetics in D1 may create a time lag that additionally allows the precursor system to relax and rearrange to more stable form, as well as impact transport of aqueous species within the pore solution. The verification of this hypothesis, together with a quantitative understanding of C-S-H crystallization mechanisms, is currently under investigation.

4.1.2 Micro and Nano-Structure

Another effect of the different partitioning of fine and coarse silica in the D-type systems relates to the micro- and nanostructure. As shown by the SANS results (Figure 7), the lower level of fine silica incorporation (D1 system) results in the development of a coarser structure of matrix comprised of nanoscale building block particles of crystalline CSH phases. The greater scattering intensity in the single-particle scattering region, as compared to the D2 system with more fine silica, indicates a greater average size of the CSH crystallites. Consequently, the void space of the D1 system matrix is dominated by large and medium capillary pores, with gel pores accounting for less than 30% of the total porosity (see Figure 13b). This internal structure seems to be not much affected by the prolonged HTHP processing, suggesting that most of the formation of the stable phases 11Å tobermorite and gyrolite took place during the first week of

curing. The D1 specimens also show a lower level of microstructure spatial homogeneity, specifically the formation of the characteristic rim of CSH product around the coarse silica particles, as compared to the D2 system. (Figure 12a).

The system with greater amount of fine silica (D2) displays a lower degree of crystallinity, as well as a much finer morphology of the nanoscale building blocks, resulting in significantly higher specific surface area (Figure 7, Table 2). This microstructural development results from kinetic reaction control, where the internal processes take place at higher rates due to the significantly increased surface area of the silica. As a result of the finer particle size of the semi-crystalline CSH, the hydrated matrix is more homogeneous and the pore space is dominated by gel pores that account for more than 90% of total porosity after 1 week of hydrothermal curing. After 3 months of curing at 200°C, the specific surface area increases slightly, indicating a still ongoing pozzolanic reaction. The prolonged curing also slightly increases the amount of medium-size capillaries, although the matrix is still dominated by gel porosity. This nanotexture is quite different from that of the D1 system, as well as from conventional HTHP cement systems where only medium-sized quartz (d_{50}<20μm) was used [5, 6]. In the latter case, one week of similar HTHP curing generated a matrix with the majority of the porosity occupied by medium and large capillary pores (see Figure 1b).

4.2 Effects of SVF and Curing Time on Microstructure Coarsening

The solid volume fraction (or, conversely, the water/solids ratio, w/s) is the most important and fundamental parameter in a cement mix design. This parameter is of critical importance as it influences the rheological properties of the cement slurry, determines the free space available for the precipitation of hydration products, and impacts the total porosity and pore size distribution

618 of the hardened paste [21, 33]. Through its effect on porosity, it also has a strong effect on the
619 mechanical properties. Of specific interest here is the important effect that the SVF has on aging
620 and microstructure coarsening of cement subjected to hydrothermal curing.

621 The investigation of the T system specimens (Ca/Si = 0.83, Table 1) revealed several important
622 effects of the SVF on the short term microstructure evolution (up to 1 week). An increased SVF
623 (i.e., a lower w/s) resulted in: a) inhibition of the C-S-H to 11Å tobermorite conversion, b) a
624 finer and more defective structure of tobermorite crystallites, and c) a reduction in capillary
625 porosity in favor of gel porosity and reduced tendency for pore domain coarsening.

626 Evidence for reduced transformation to tobermorite at higher SVF was provided by the XRD
627 results shown in Figure 4. We hypothesize that the conversion of C-S-H to tobermorite tends to
628 be suppressed when there is less free volume available for the precipitation of the hydration
629 products. This is also supported by the XRD results for the D1 and D2 systems with bimodal
630 silica additive incorporation (Figure 3a-b). Note that both the D2 and T systems incorporate fine
631 silica of very comparable granulometry (Figure 2) and in similar amounts. However, the D2
632 system has a considerably higher SVF than all of the T-system specimens (Table 1). Therefore,
633 more pronounced suppression of C-S-H-to-tobermorite conversion takes place at higher SVF and
634 tends to span over longer time frame.

635 This observation of suppressed C-S-H-to-tobermorite conversion at higher SVF is also supported
636 by a recent study by Kikuma et al. [66]. These authors showed formation of semi-crystalline C-
637 S-H instead of 11Å tobermorite in high SVF (low w/s) mixtures, while increasing the amount of
638 water facilitated its formation. On the other hand, prolonged hydrothermal treatment resulted in
639 increased tobermorite crystallization, regardless of the initial water content of the mix. However,

as discussed earlier, the rate of this conversion process appears to be strongly linked to the amount of free space available for crystallization.

The initial SVF also appears to impact the size and crystalline structure of the newly forming tobermorite crystallites. Regardless of the processing time, increasing the SVF leads to enhanced peak broadening of the tobermorite diffraction lines (see Figure 5), which can be assumed to result from a reduction in size and/or increased number of defects in the crystal lattice. In future investigations it will be useful to consider the combination of SVF, quartz particle size, and curing schedule that creates the unique chemical conditions in the highly confined pore solution environment to support this phenomenon.

Finally, another important effect of SVF on the cement microstructure relates to the pore size distribution. When HTHP curing begins, the pozzolanic reaction of the quartz causes new hydration product to fill the capillary space established by precuring of the cement at ambient temperature, creating an HTHP microstructure dominated by gel porosity. However, a systematic offset in the pore structure remains: as the SVF decreases, an increasing amount of capillary pore volume is filled with a similar amount of HTHP hydration product. This effect is completely analogous to the impact of w/c ratio on the pore structure of ordinary cement paste, where a higher fraction of medium and capillary voids is created by increasing water content of the mix [21, 33]. Lastly, we note that pore structure coalescence tends to be inhibited with increasing SVF (see Figure 14b,c). This fact, together with the negligible effect of curing time on the total porosity and skeletal density of the model matrices (Table 5), indicates that pore coalescence (microstructure coarsening) results mainly from growth of 11Å tobermorite crystals.

5. SUMMARY AND CONCLUSIONS

The effects of hydrothermal high-temperature curing at 200ºC on Class G portland cement blended with crystalline silica were studied. The specific variables that were explored were: the total amount of silica, the partitioning between fine and coarse silica powders, and the solid volume fraction of the mix design. After curing, the phase composition, matrix chemical composition, total porosity, pore size distribution, and the size of the fundamental nanoscale particles of crystalline and semi-crystalline C-S-H phases were characterized. These experimental observations revealed significant differences in the final phase assembly of the CSH matrix. Gyrolite and 11Å tobermorite coexist and are dominant in the cement system containing the lower fraction (15% bwoc) of fine silica, while semi-crystalline C-S-H was dominant when the greater fraction (25% bwoc) of fine silica was used.

Incorporation of a greater amount of fine silica resulted in significantly reduced dissolution of the coarse silica particles and improved the homogeneity of the microstructure. We attribute these effects to different hydrothermal reaction mechanisms taking place at the local scale of material microstructure, resulting in either thermodynamic or kinetic reaction control. These two modes of reaction control also result in differences in the pore structure of the HTHP cement matrix. When the matrix contains primarily semi-crystalline C-S-H, the porosity is dominated by gel pores. In the presence of crystalline CSH phases (such as tobermorite or gyrolite) the porosity is coarser and is dominated by medium and large capillary pores.

As indicated by the XRD results, lower values of SVF (i.e., greater initial porosity) leads to more rapid formation of 11Å tobermorite at the expense of its precursor, C-S-H gel. As a result, specimens with lower SVF exhibit a greater degree of crystallinity and/or greater crystallite size. Prolonged duration of HTHP curing of all systems (up to three months in this study), irrespective

of the initial SVF, increases the fraction of capillary pores, indicating void coalesce caused by crystal growth. However, this coarsening effect is less pronounced in systems with higher SVF. The transformation of C-S-H into tobermorite appears to be suppressed when there is less free volume in the microstructure.

6. ACKNOWLEDGEMENT

The authors would like to acknowledge the support of Schlumberger through a previous Schlumberger-MIT cement research collaboration, X-Cem. We also would like to thank the Concrete Sustainability Hub at MIT, with sponsorship provided by the Portland Cement Association (PCA) and the RMC Research & Education Foundation. The authors are grateful for this support.

7. REFERENCES

[1] G. DeBruijn, C. Skeates, R. Greenway, D. Harrison, M. Parris, S. James, F. Mueller, S. Ray, M. Riding, L. Temple, K. Wutherich, High-Pressure, High-Temperature Technologies, Oilfield Review, 20(2008), pp. 46-60

[2] E. B. Nelson and D. Guillot, Well Cementing, second ed., Schlumberger, 2006.

[3] C. Menzel, Strength and volume change of steam cured concrete, ACI Proc., 31 (1934), pp. 125-149

[4] L. Eilers, R. Root, Long-term effects of high temperature on strength retrogression of cements, *Soc. Pet. Eng.*, 5028 (1974)

[5] K. J. Krakowiak, J. J. Thomas, S. Musso, A. -T. Akono and F. -J. Ulm, Nano-chemo-mechanical signature of conventional oil-well cement systems: Effects of elevated

temperature and curing time, Cem. Concr. Res., 67 (2015), pp. 103-121

[6] J. J. Thomas, S. James, J. A. Ortega, S. Musso, F. Auzerais, K. J. Krakowiak, A. T. Akono, F. -J. Ulm, R. Pellenq, Fundamental Investigation of the Chemical and Mechanical Properties of High-Temperature-Cured Oilwell Cements, Offshore Technology Conference, OTC-23668-MS,30 April-3 May, Houston, Texas, USA.

[7] I. G. Richardson, The calcium silicate hydrates, Cem. Concr. Res., 38 (2008), pp. 137-158

[8] A.K. Chatterjee, X-Ray Diffraction in: V. S. Ramachandran, J. J. Beaudoin, Handbook of analytical techniques in concrete science and technology: principles, tehcniques, and applications, Noyes Publications, William Andrew Publishing, LLC, 2001, pp. 275-333.

[9] S. Howard, K. Preston, Profile fitting of powder diffraction patterns, Rev. Mineral. Geochem., 20 (1989), pp. 217-275

[10] R. Young, The Rietveld Method, Oxford Science Publications, 1995.

[11] S. Speakman, Profile Ditting for Analysis of XRPD Data using HighScore Plus, Center for Materials Science and Engineering, MIT, Lecture Notes, http://prism.mit.edu/xray/

[12] D. Black, D. Windover, A. Henins, J. Filliben, J. Cline, Standard reference material for x-ray metrology in: *Advances in x-ray analysis, proceedings of the Denver X-ray Conference, 2012, Vol. 54*, 2010.

[13] J. J. Thomas, H. M. Jennings, A. J. Allen, The surface area of hardened cement paste as measured by various techniques, Cem. Concr. Res., 1 (1999), pp. 45-64

[14] A. J. Allen, J. J. Thomas, H. M. Jennings, Composition and density of nanoscale calcium-silicate-hydrate in cement, Nat. Mater., 6 (2007), pp. 311-316

[15] J. J. Thomas, A. J. Allen, H. M. Jennings, Density and water content of nanoscale solid C-S-H formed in alkali-activated slag (AAS) paste and implications for chemical shrinkage, Cem. Concr. Res., 42 (2012), pp. 377-383

[16] J. J. Thomas, H. M. Jennings, A. J. Allen, Relationships between composition and density of tobermorite, jennite and nanoscale CaO-SiO2-H2O, J. Phys. Chem. C, (2010), pp. 7594-7601

[17] J. Armstrong, A package of correction programs for the quantitative electron microbeam X-ray analysis of think polished materials, thin films, and particles, Microbeam Anal., 4 (1995), pp. 177-200

[18] J. Armstrong, D. Newbury, L. Lifshin et.al., Quantitative X-ray Microanalysis:Problem Solving Using EDS and WDS Techniques, Lecture Notes, Lehigh Microscopy School, 2012.

[19] J. Goldstein, D. Newbury, D. Joy, C. Lyman, P. Echlin, E. Lifshin, L. Sawyer, J. Michael, Scanning Electron Microscopyand x-ray Microanalysis, third ed., Springer, New York, 2008.

[20] G. J. McLachlan, D. Peel, Finite Mixture Models, Wiley-Interscience, 2000.

[21] S. Mindes, J. F. Young, D. Darein, Concrete, second ed., Prentice Hall, 2002.

[22] J. J Thomas, H. M. Jennings, Pyknometry (pore volume) measurements of cement paste, in The science of concrete, http://iti.northwestern.edu/cement/monograph/Monograph7_4.html

[23] H. F. W. Taylor, Bound water in cement pastes and its significance for pore solution compositions, MRS Proceedings, 85 (1986), pp. 47-54

[24] A. E. Moore, H. F. W. Taylor, Crystal structure of ettringite, Nature, 218 (1968), pp. 1048-1049

[25] N. Skoblinskaya, K. Krasilnikov, Changes in crystal structure of ettringite on dehydration.1, Cem. Concr. Res., 5 (1975), pp. 381-394

[26] N. Skoblinskaya, K. Krasilnikov, L. Nikitina, V. Varlamov, Changes in crystal structure of ettringite on dehydration. 2, Cem. Concr. Res., 5 (1975), pp. 419-432

[27] S. Merlino, E. Bonaccorsi, T. Armbruster, The real structure of tobermorite 11A: normal and anomalous forms, OD character and polytypic modifications, Eur. J. Mineral., 13 (2001), pp. 577-590

[28] S. Grangeon, F. Claret, C. Lerouge, F. Warmont, T. Sato, S. Anraku, C. Numako, Y. Linard, B. Lanson, On the nature of structural disorder in calcium silicate hydrates with a calcium/silicon ratio similar to tobermorite, Cem. Concr. Res., 52 (2013), pp. 31-37

[29] S. Grangeon, F. Claret, Y. Linard, C. Chiaberge, X-ray diffraction: a powerful tool to probe and understand the structure on nanocrystalline calcium silicate hydrates, Acta Crystallogr. Sect. A, 69 (2013), pp. 465-473

[30] S. Shaw, C. Henderson, S. Clark, In-situ synchrotron study of the kinetics, thermodynamics, and reaction mechanisms of the hydrothermal crystallization of gyrolite, Ca16S24O60(OH)8*14H2O, Am. Mineral., 87 (2002), pp. 533-541

[31] J. Chen, J. J. Thomas, H. F. W. Taylor, H. M. Jennings, Solubility and structure of calcium silicate hydrate, Cem. Concr. Res., 34 (2004), pp. 1499-1519

[32] J. R. Houston, R. S. Maxwell, S. A. Carroll, Transformation of meta-stable calcium silicate hydrates to tobermorite: reaction kinetics and molecular structure from XRD and NMR spectroscopy, Geochem. Trans., 10 (2009)

[33] H. F. W. Taylor, Cement Chemistry, Thomas Telford, 1997.

[34] F. H. Chung, Quantitative interpretation of X-ray diffraction patterns of mixes: I. Matrix-Flushing Method for quantitative multicomponent analysis, J. Appl. Crystallogr., 7 (1974), pp. 519-525

[35] H. Klug, L. Alexander, X-ray diffraction procedures for polycrystalline and amorphous materials, John Wiley & Sons, 1974.

[36] B. E. Warren, X-ray diffraction, Addison-Wesley, 1969.

[37] P. Scherrer, Bestimmung der grosse und der inneren struktur von kolloidteilchen mittels rontgenstrahlen, *Nachr. Ges. Wiss. Gottingen,* 26 (1918), pp. 98-100

[38] J. Langford, A. Wilson, Scherrer after sixty years: A survey and some new results in the determination of crystallite size, *J. Appl. Cryst.,* 11 (1987), pp. 102-113

[39] S. Shaw, S. Clark, C. Henderson, Hydrothermal formation of the calcium silicate hydrates, tobermorite Ca5Si6O16(OH)2(H2O)4 amd xonotlite Ca6Si6O17(H2O)2: an in situ synchrotron study, Chem. Geol., 167 (2000), pp. 129-140

[40] H. M. Jennings, J. J. Thomas, J. S. Gevrenov, G. Constantinides, F.-J. Ulm, A multi-technique investigation of the nanoporosity of cement paste, Cem. Concr. Res., 37 (2007), pp. 329-336

[41] I. G. Richardson, Tobermorite/jennite- and tobermorite/calcium hydroxide-based models for the structure of C-S-H: applicability to hardened pastes of tricalcium silicate, beta-dicalcium silicate, Portland cement, and blends of Portland cement with blast-furnace slag, metakaolin, or silica fume , Cem. Concr. Res, 34 (2004), pp. 1733-1777

[42] H. S. Wong, N. R. Buenfeld, Monte Carlo simulation of electron-solid interactions in cement-based materials, Cem. Concr. Res., 36 (2006), pp. 1076-1082

[43] S. Diamond, J. White, W. Dolch, Effects of isomorphous substitution in hydrothermally synthesized tobermorite, Am. Mineral., 51 (1966), pp. 388-401

[44] G. L. Kalousek, Crystal chemistry of hydrous calcium silicates: I, substitution of aluminum in lattice of tobermorite, J. Am. Ceram. Soc., 40 (1957), pp. 74-80

[45] S. A. S. El-Hemaly, T. Mitsuda, H. F. W. Taylor, Synthesis of normal and anomalous tobermorite, Cem. Concr. Res., 7 (1977), pp. 429-438

[46] M. W. Barnes, B. E. Scheetz, The chemistry of Al-tobermorite and its coexisting phases at 175C, MRS Proceedings, 179 (1991)

[47] E. P. Flint, H. F. McMurdie, L. S. Wells, Hydrothermal and x-ray studies of the garnet-hydrogarnet series and the relationship of the series to hydration products of Portland cement, J. Res. Natl. Bur. Stand., 26 (1941), pp. 13-33

[48] K. Kyritsis, N. Meller, C. Hall, Chemistry and morphology of hydrogarnets formed in cement-based CASH hydroceramics cured at 200°C to 350°C, J .Am. Ceram. Soc., 92 (2009), pp. 1105-1111

[49] N. Meller, K. Kyritsis, C. Hall, The mineralogy of the CaO-Al_2O_3-SiO_2-H_2O (CASH) hydroceramic system from 200 to 350°C, Cem. Concr. Res., 39 (2009), pp. 45-53

[50] R. M. German, Particle Packing Characteristics, Metal Powder Industries Federation, 1989.

[51] R. A. Cook, K. C. Hover, Mercury porosimetry of hardened cement pastes, Cem. Concr. Res., 29 (1999), pp. 933-943

[52] S. A. Greenberg, Reaction between slica and calcium hydroxide solutions. I. Kinetics in the temperature range 30 to 80°C, J. Phys. Chem, 65 (1961), pp. 12-16

[53] D. R. Moorehead, E. R. McCartney, Hydrothermal formation of calcium silicate hydrates, J .Am. Ceram. Soc., 48 (1965), pp. 656-569

[54] C. F. Chan, M. Sakiyama, T. Mitsuda, Kinetics of the CaO-Quartz-H_2O reaction at the 120 to 180°C in suspensions, Cem. Concr. Res., 8 (1978), pp. 1-6

[55] S. Bernstein, Determination of reaction kinetics and mechanisms of 1.13nm tobermorite by in-situ neutron diffraction, PhD dissertation, Ludwig Maximilian University of Munich, 2011, https://edoc.ub.uni-muenchen.de/14384/

[56] S. Bernstein, K. T. Fehr, The formation of 1.13 nm tobermorite under hydrothermal conditions: 1. The influence of quartz grain size within the system CaO–SiO_2–D_2O," Prog. Cryst. Growth Charact. Mater., 58 (2012), pp. 84-91

[57] L. Bruner, St. Tolloczko, Uber die Auflosungsgeschwindigkeit fester korper, Z. Phys.

Chem, 35 (1900), pp. 283-290

[58] A. Dokoumetzidis, P. Macheras, A century of dissolution research: from Noyes and Whitney to the biopharmaceutics classification system, Int. J. Pharm, 321 (2006), pp. 1-11

[59] A. A. Noyes, W. R. Whitney, The rate of solution of solid substances in their own solutions, J. Am. Chem. Soc., 19 (1897), pp. 930-934

[60] B. Lothenbach, A. Nonat, Calcium silicate hydrates: solid and liquid phase composition, Cem. Concr. Res., 78 (2015), pp. 57-70

[61] T. Peters, Comparative study of the use of quartz poor sand and pure quartz sand for lime silica bricks and the kinetics of the hydrothermal hardening mechanicsm, Cem. Concr. Res., 8 (1978), pp. 415-424

[62] S. O. Oyefesobi, D. M. Roy, Hydrothermal studies of type V cement-quartz mixes, Cem. Concr. Res., 6 (1976), pp. 803-810

[63] H. F. W. Taylor, The calcium silicate hydrates, in: H. F. W. Taylor (Ed.), The Chemistry of Cements, vol. 1, Academic Press, London, pp. 168-232, 1964.

[64] D. A. Buckner, D. M. Roy, R. Roy, Studies in the system CaO-Al_2O_3-SiO_2-H_2O, II: The system $CaSiO_3$-H_2O, Am. J. Sci., 258 (1960), pp. 132-147

[65] N. Isu, H. Ishida, T. Mitsuda, Influence of quartz particle size on the chemical and mechanical properties of autoclaved aerated concrete (I) tobermorite formation, Cem. Concr. Res., 25 (1995), pp. 243-248

[66] J. Kikuma, M. Tsunashima, T. Ishikawa, S. Matsuno, A. Ogawa, K. Matsui, M. Sato, Effects of quartz particle size and water-to-solid ratio on the hydrothermal synthesis of tobermorite studied by in-situ time-resolved X-ray diffraction, J. Solid State Chem., 184 (2011), pp. 2066-2074

[67] E. Masoero, J. J. Thomas, H. M. Jennings, A Reaction Zone Hypothesis for the Effects of

Particle Size and Water-to-Cement Ratio on the Early Hydration Kinetics of C3S, J .Am. Ceram. Soc., 97 (2014), pp. 967-975

[68] M. P. Ginebra, F. C. M. Driessens, J. A. Planell, Effect of the particle size on the micro and nanostructure features of a calcium phospate cement: a kinetic analysis, Biomaterials, 25 (2004), pp. 3453-3462

[69] V. J. Anderson, H. N. W. Lekkerkerker, Insights into phase transition kinetics from colloid science, Nature, 416 (2002), pp. 811-815

[70] N. Rodriguez-Hornedo, D. Murphy, Significance of controlling crystallization mechanicsm and kinetics in pharmaceutical systems, J. Pharm. Sci., 88 (1999), pp. 651-660

[71] H. Sato, M. Grutzeck, Effect of starting materials on the synthesis of tobermorite, Mat. Res. Soc. Symp. Proc., 245 (1992), pp. 235-240

[72] E. E. Lachowski, S. Y. Hong, F. P. Glasser, Crystallinity in C-S-H gels: influence of preparation and cure conditions, in: A. Nonat, 2nd International RILEM Workshop on Hydration and Setting, Why does cement set? An interdisciplinary approach, Dijon, France, 1997.

[73] H. F. W. Taylor, The transformation of tobermortie into xonotlite, Mineral. Mag., 32 (1958), pp. 110-116

[74] R. Jauberthie, M. Temimi, M. Laquerbe, Hydrothermal transformation of tobermortie gel to 10Å tobermorite, Cem. Concr. Res., 26 (1996), pp. 1335-1339

FIGURES

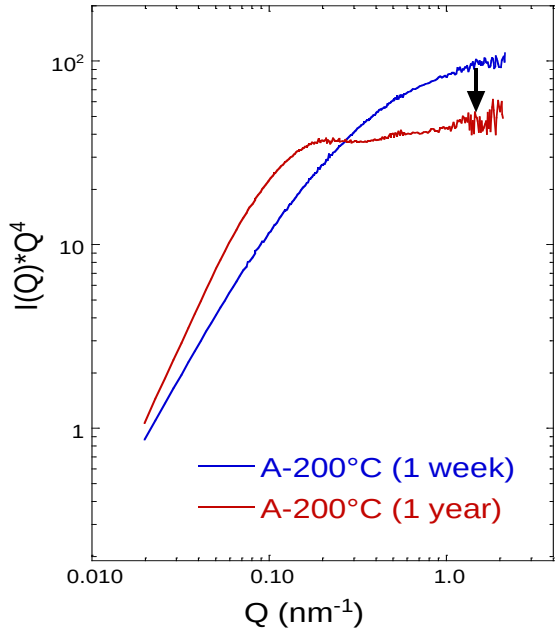

(a)

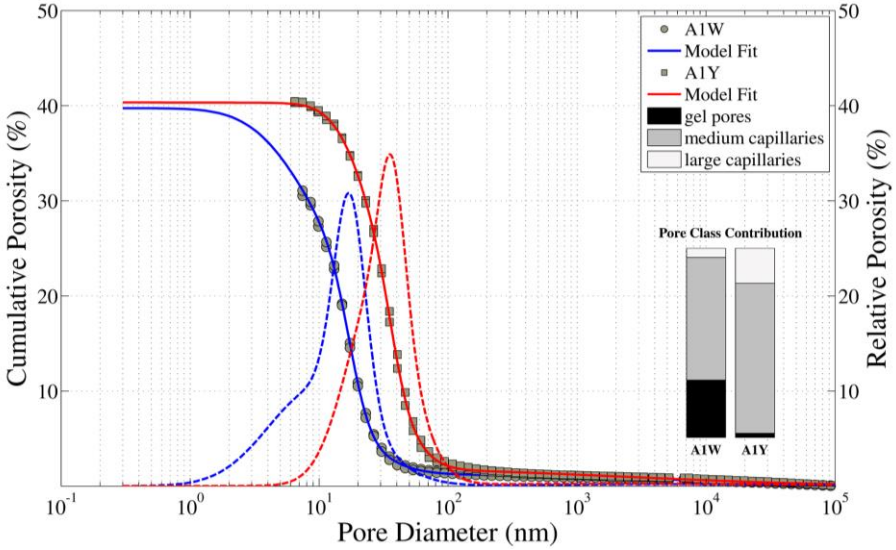

(b)

Figure 1. Coarsening of a binder consisting of Class G cement with 35% bwoc silica flour and exposed to hydrothermal curing at 200ºC for one week (A1w) or one year (A1y), after [5]. a) Small-angle neutron scattering (SANS) results showing a decrease in the scattered intensity at the highest Q-values (marked by a downward arrow), which indicates a reduction in the specific surface area, SSA. The horizontal shift of the high-Q Porod scattering regime with time toward lower Q-values indicates the growth of the smallest solid features generating scattering. b) Mercury Intrusion Porosimetry (MIP) results showing an increase in the median pore diameter and a significant reduction of the gel porosity in favor of medium and large capillaries with time.

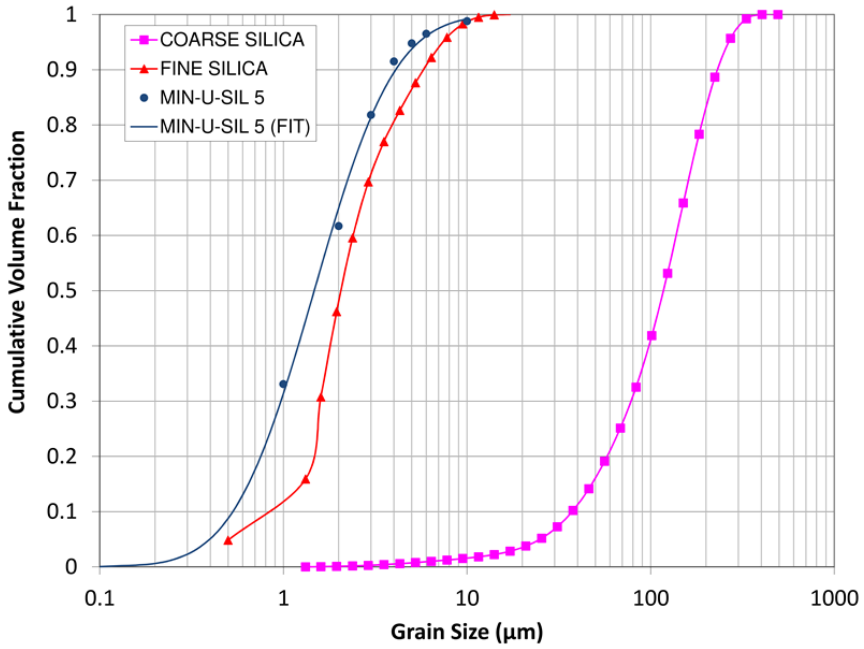

Figure 2. Particle size distributions of the silica powders used in this study. Particle size distribution of MIN-U-SIL®5 (US Silica) extrapolated with CDF function in the d<1µm range.

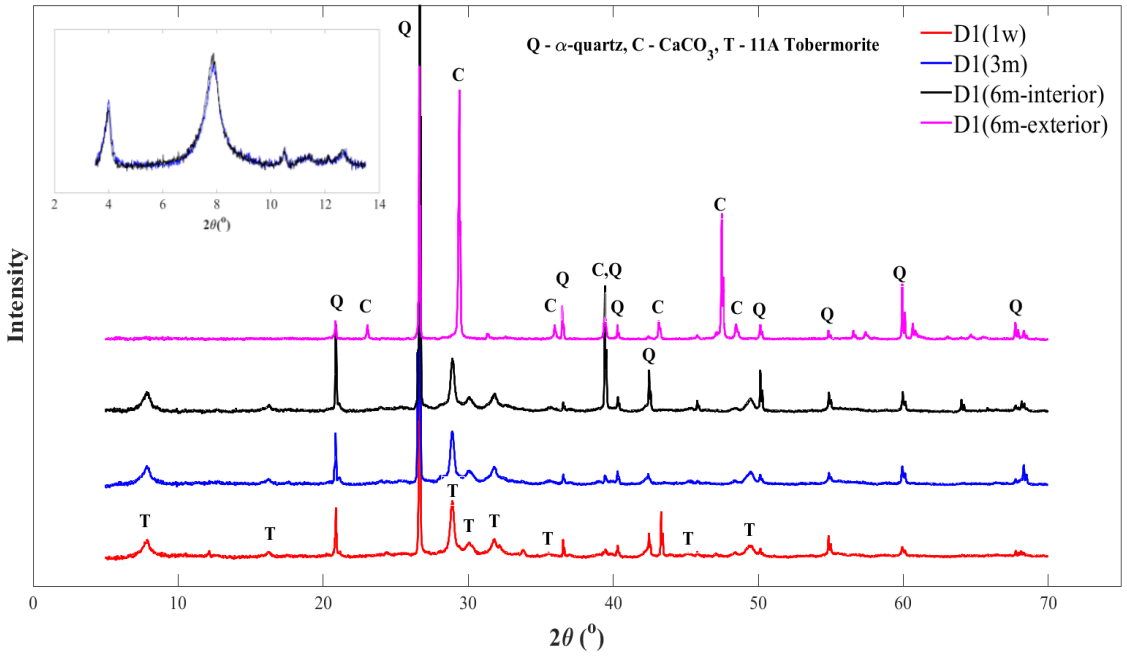

(a)

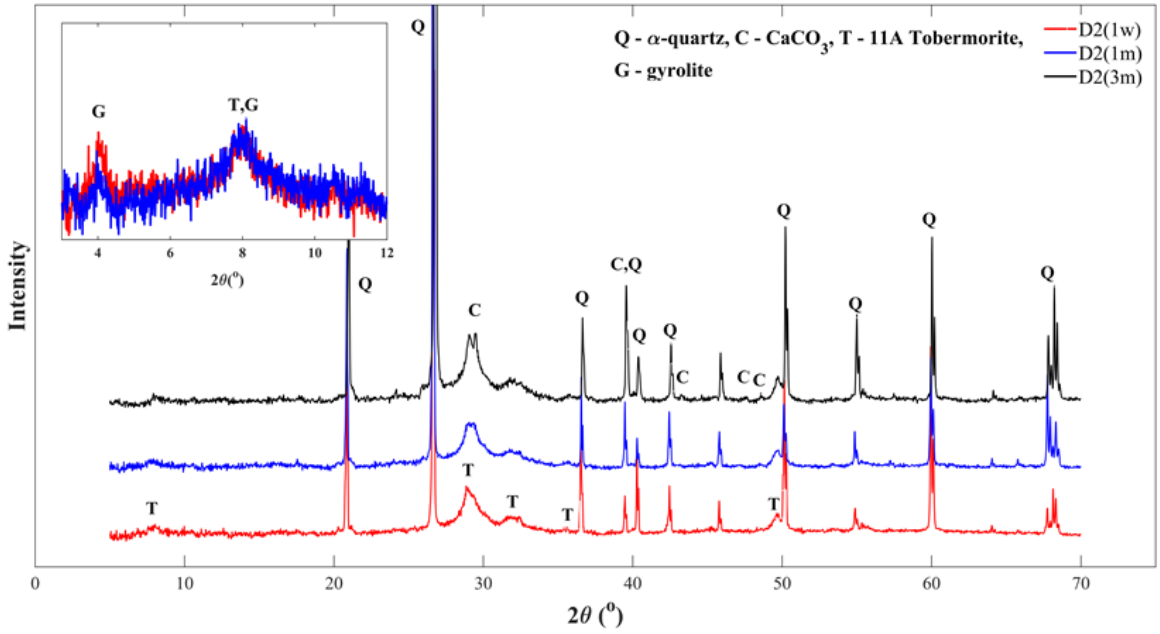

(b)

Figure 3. X-ray powder diffraction spectra with qualitative phase assessment for D-system specimens cured hydrothermally at 200°C. (a) System D1 cured from 1 week, 3 months, and 6 months, (b) System D2 cured for 1 week, 1 month, and 3 months.

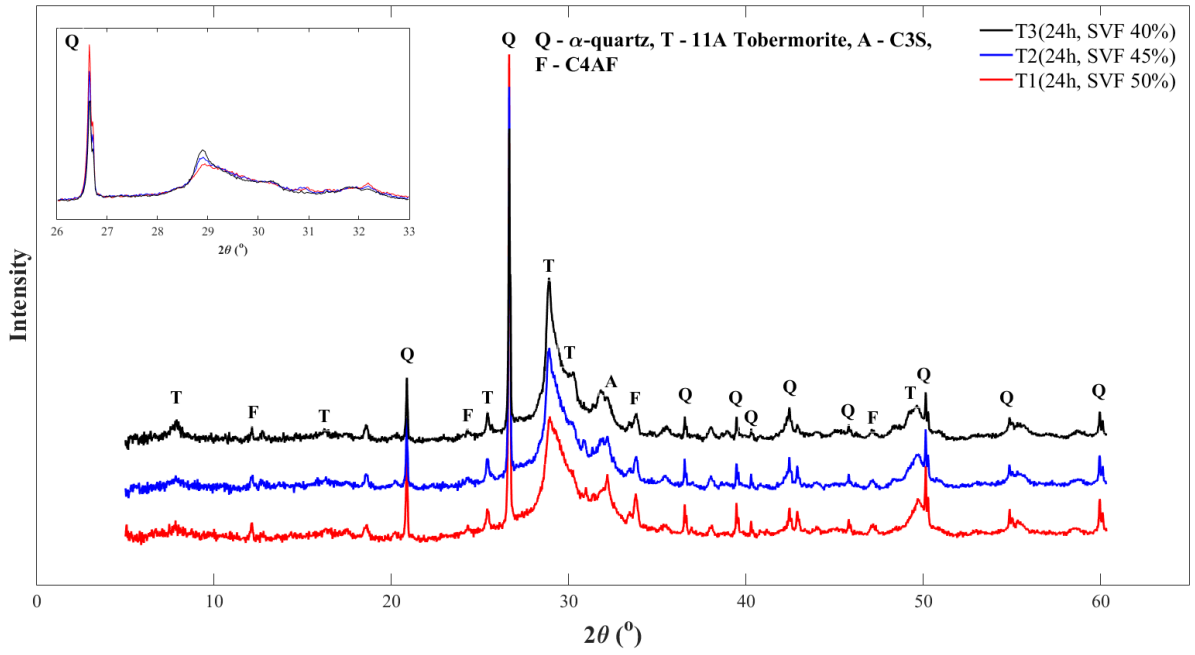

(a)

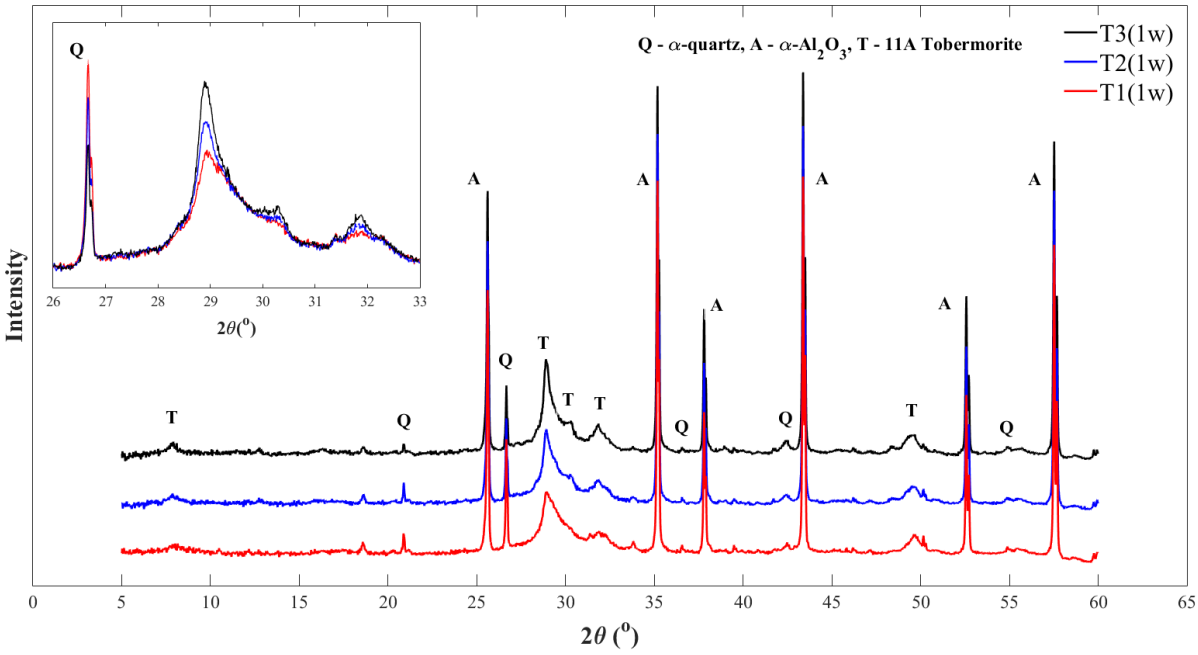

(b)

Figure 4. X-ray powder diffraction spectra for system T specimens with different SVF values, with qualitative phase assessment of major components. (a) Cured for 24 h at 200°C. (b) Cured for 1 week at 200°C, and normalized with respect to internal corundum standard (α-Al_2O_3) added in all samples in the amount of 30% wt.

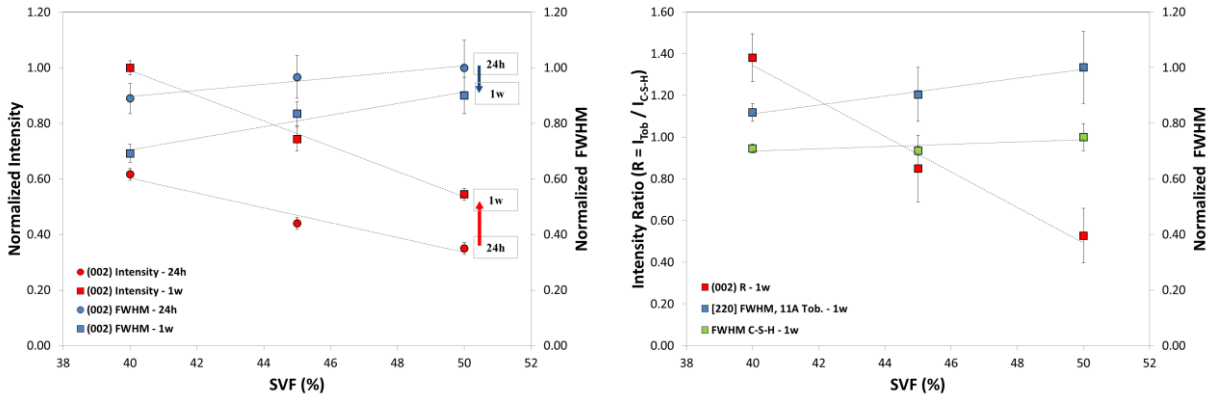

(a) (b)

Figure 5. Effect of SVF on the phase distribution in the T-system samples. (a) Relative intensity, I, and full width at half maximum (FWHM) of the (002) 11Å tobermorite basal reflection. (b) Intensity ratio, R, FWHM of (220) tobermorite reflection and 3.06Å C-S-H diffraction band.

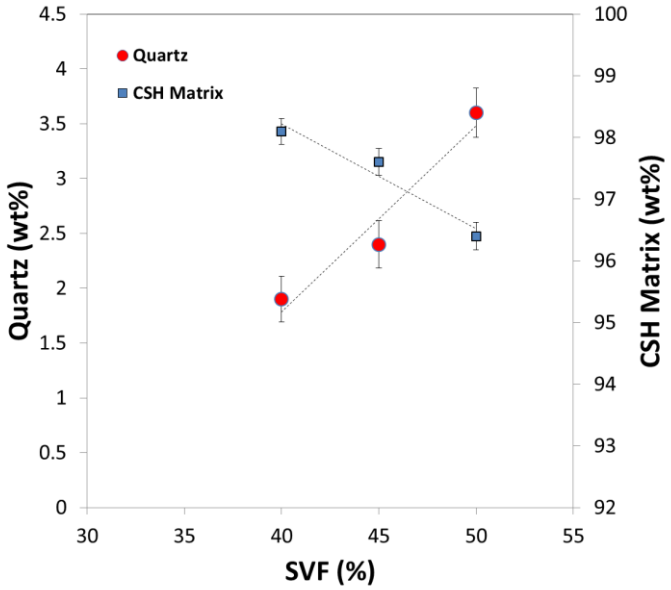

Figure 6. Weight fractions of α-quartz and CSH matrix (the sum of amorphous C-S-H and crystalline CSH phases), with respect to the solid volume fraction (SVF) of the T-system specimens cured hydrothermally for 1 week. Quantitative results obtained with Rietveld refinement method. Error bars represent 95% confidence intervals derived from the refinement analysis.

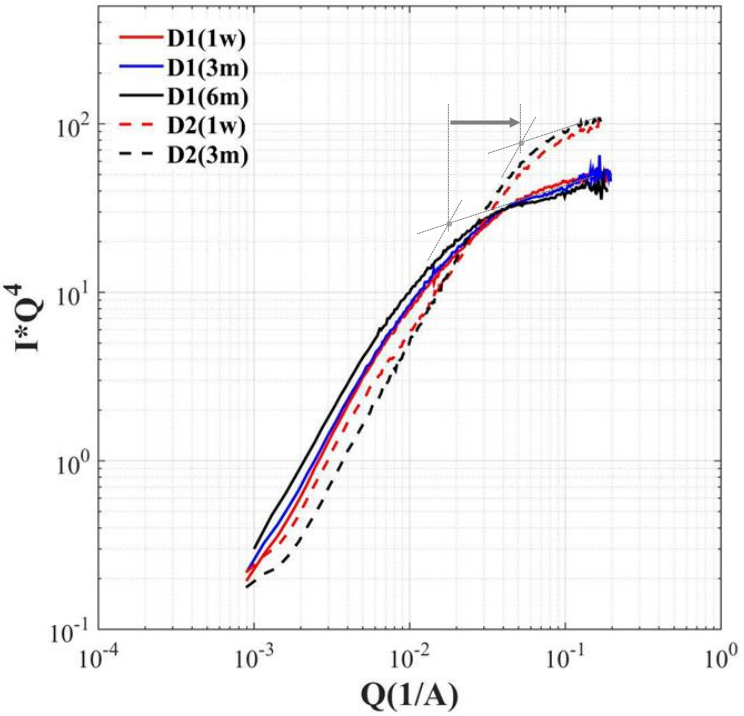

Figure 7. SANS response of the systems D1 and D2 cured at 200°C from 1 week to 6 months. The arrows indicate a shift toward a smaller size of the nano-scale solid features generating much greater scattering in the single-particle scattering regime in the D2 specimens than in D1.

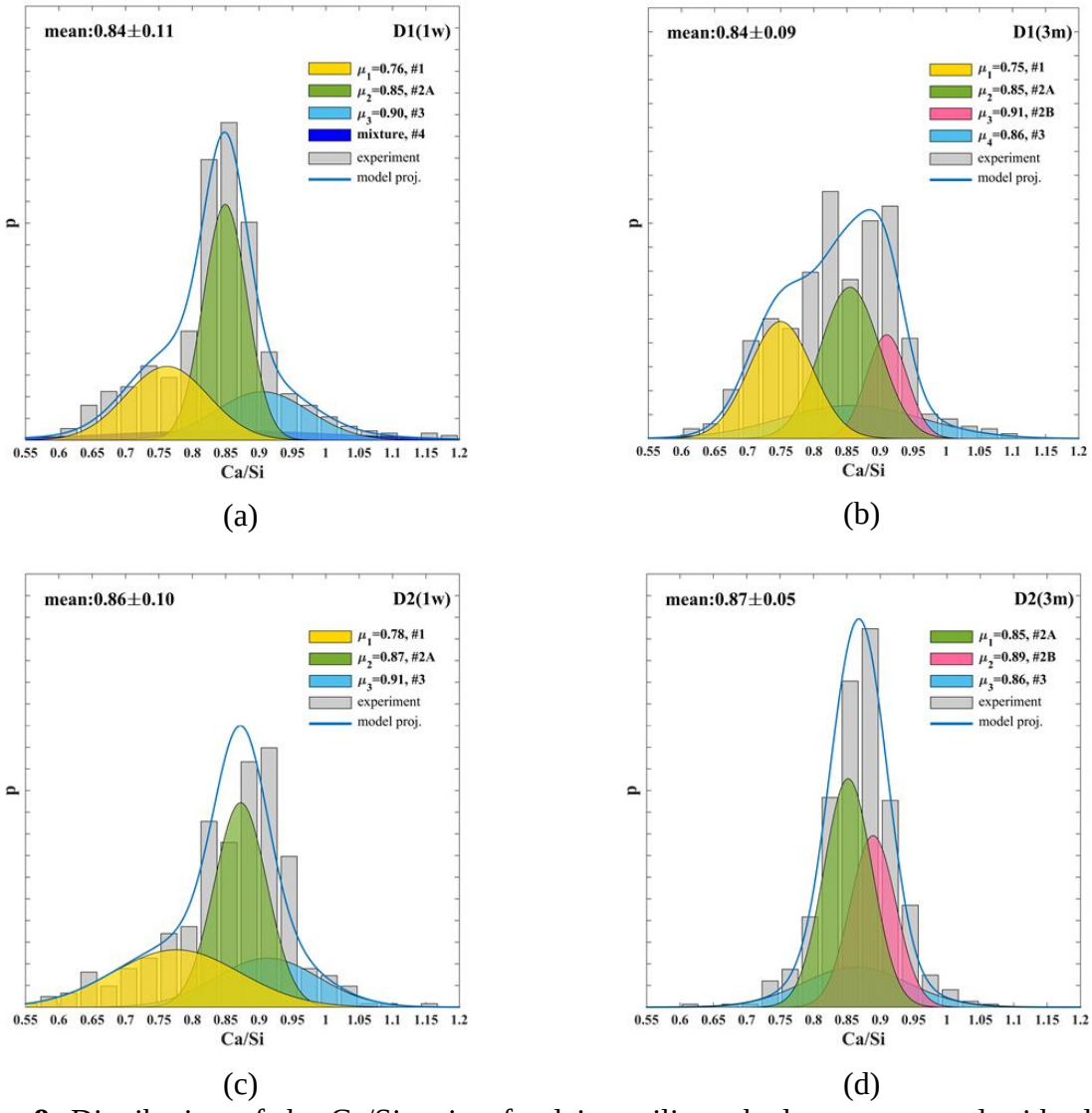

Figure 8. Distribution of the Ca/Si ratio of calcium silicate hydrates measured with electron probe microanalysis in: a-b) system D1, c-d) system D2, cured from 1 week to 3 months. Error on the mean value of Ca/Si ratio corresponds to one standard deviation.

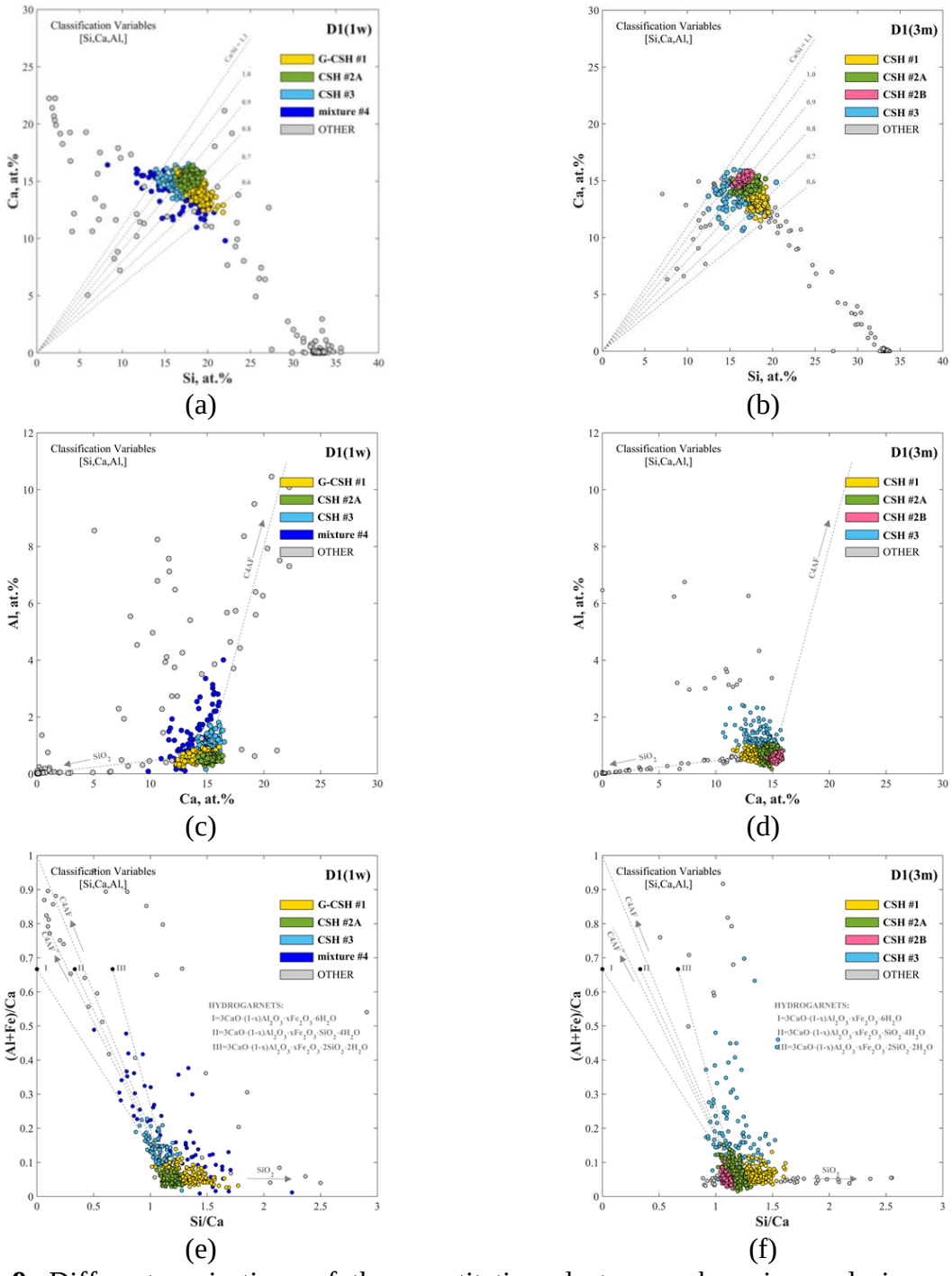

Figure 9. Different projections of the quantitative electron probe microanalysis results for system D1: (a,c,e) after 1 week of hydrothermal curing, (b,d,f) after 3 months of hydrothermal curing. Phase inference and clustering achieved assuming Gaussian Mixture Modelling and Bayes rule of allocation [5, 20].

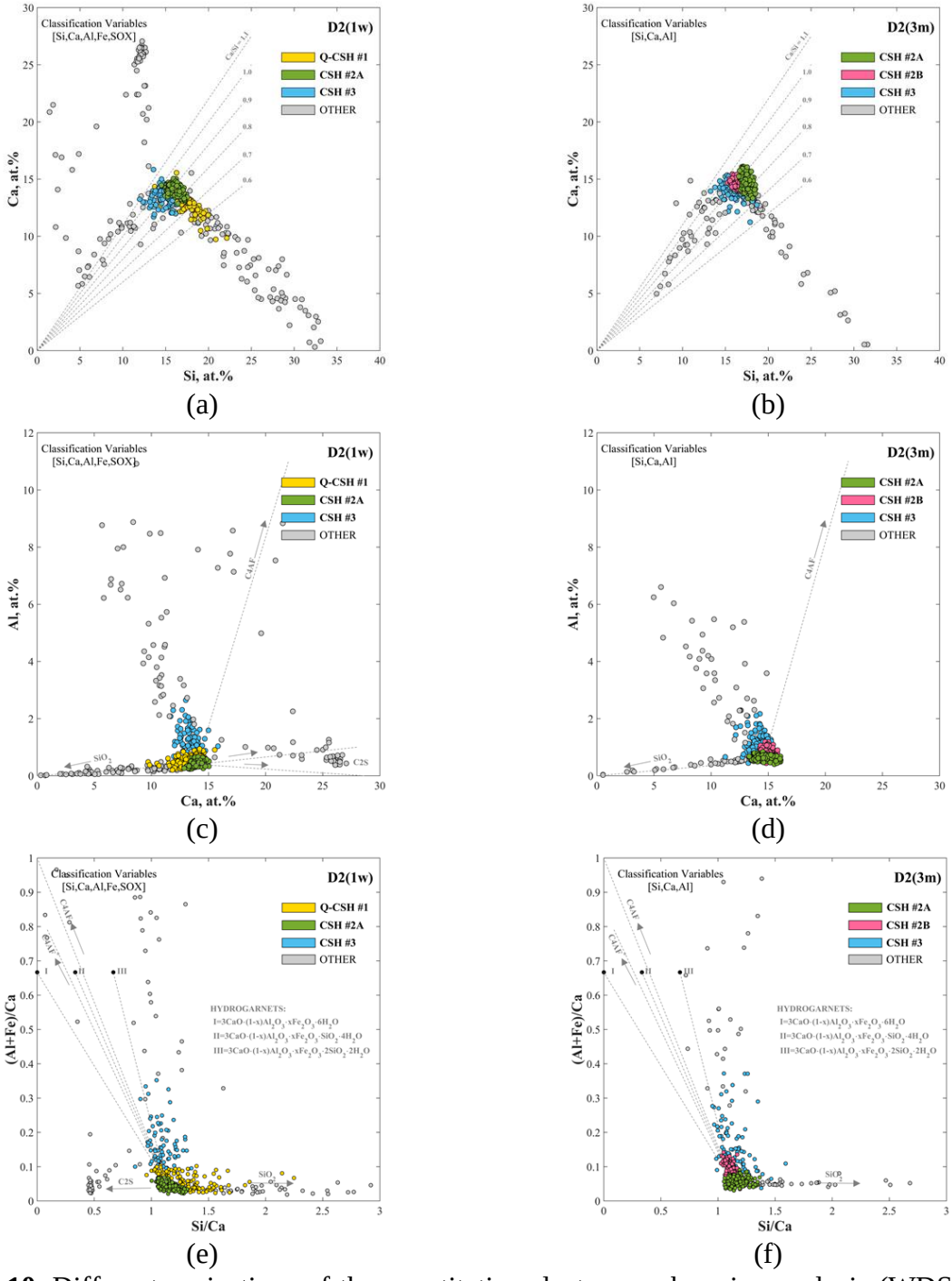

Figure 10. Different projections of the quantitative electron probe microanalysis (WDS) results for system D2: (a,c,e) after 1 week of hydrothermal curing, (b,d,f) after 3 months of hydrothermal curing. Phase inference and clustering achieved assuming Gaussian Mixture Modelling and Bayes rule of allocation [5, 20].

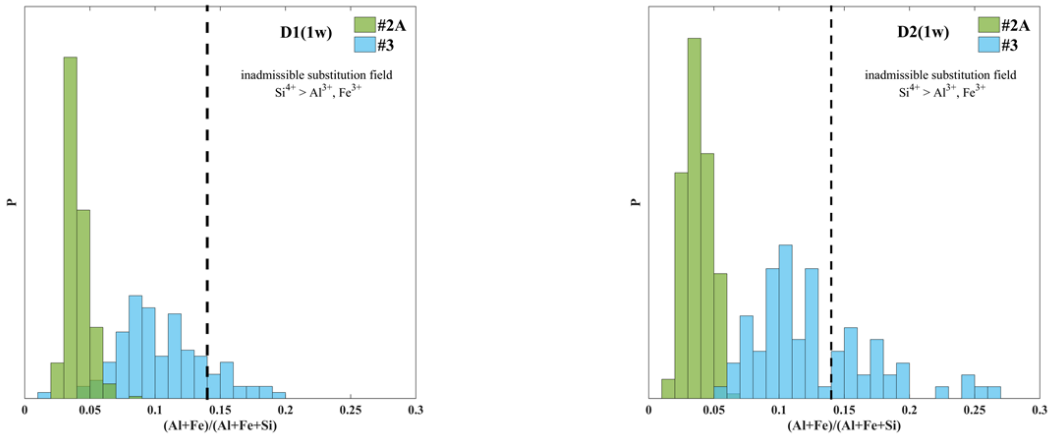

(a) (b)

Figure 11. Frequency diagrams of the (Al+Fe)/(Al+Fe+Si) atomic ratio calculated for the observations in group #2A and #3: (a) sample D1(1w), (b) sample D2(1w).

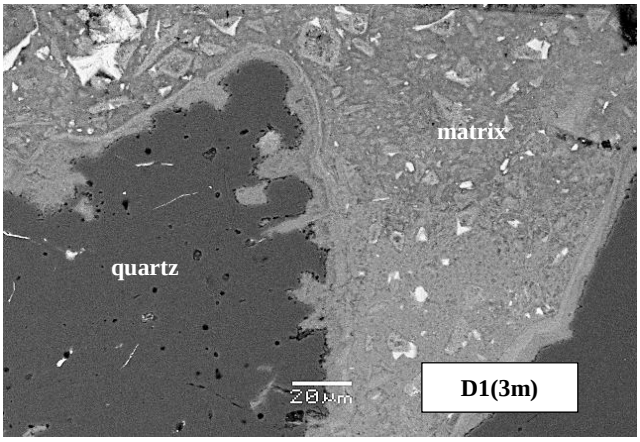

(a)

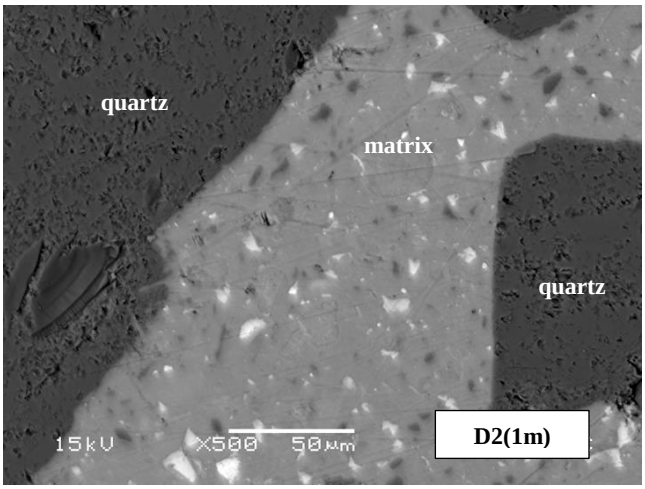

(b)

Figure 12. BSE micrographs of D1 and D2 systems: (a) an example of partially reacted coarse particle of quartz with characteristic reaction rim and complete reaction of fine silica material in D1 type matrix, (b) matrix of D2 system with residual fine silica material and sound boundaries of coarse particles.

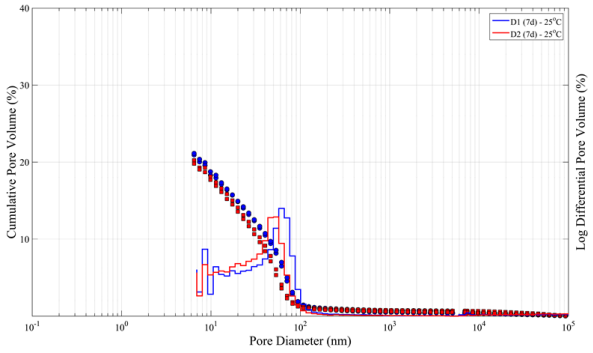

(a)

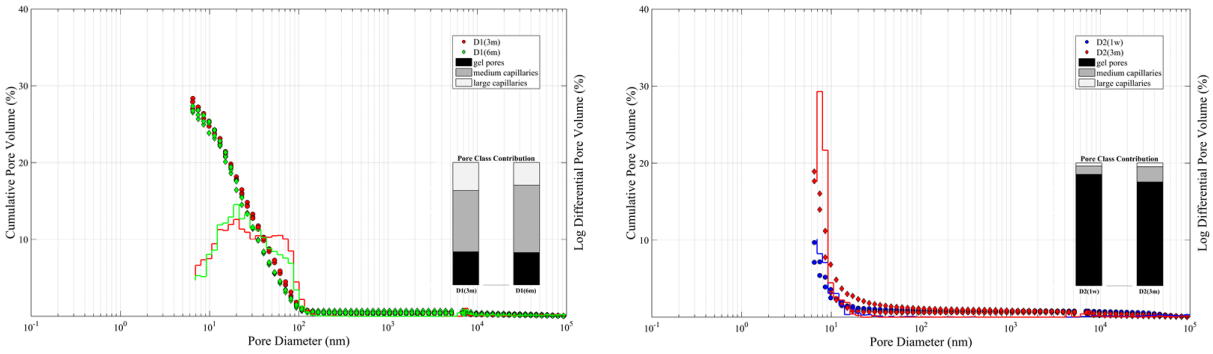

(b) (c)

Figure 13. Cumulative intrusion curves and pore size distributions obtained on a) system D1 and D2 aged for 1 week at 25°C, b) system D1, and c) system D2, exposed to prolonged hydrothermal treatment at 200°C.

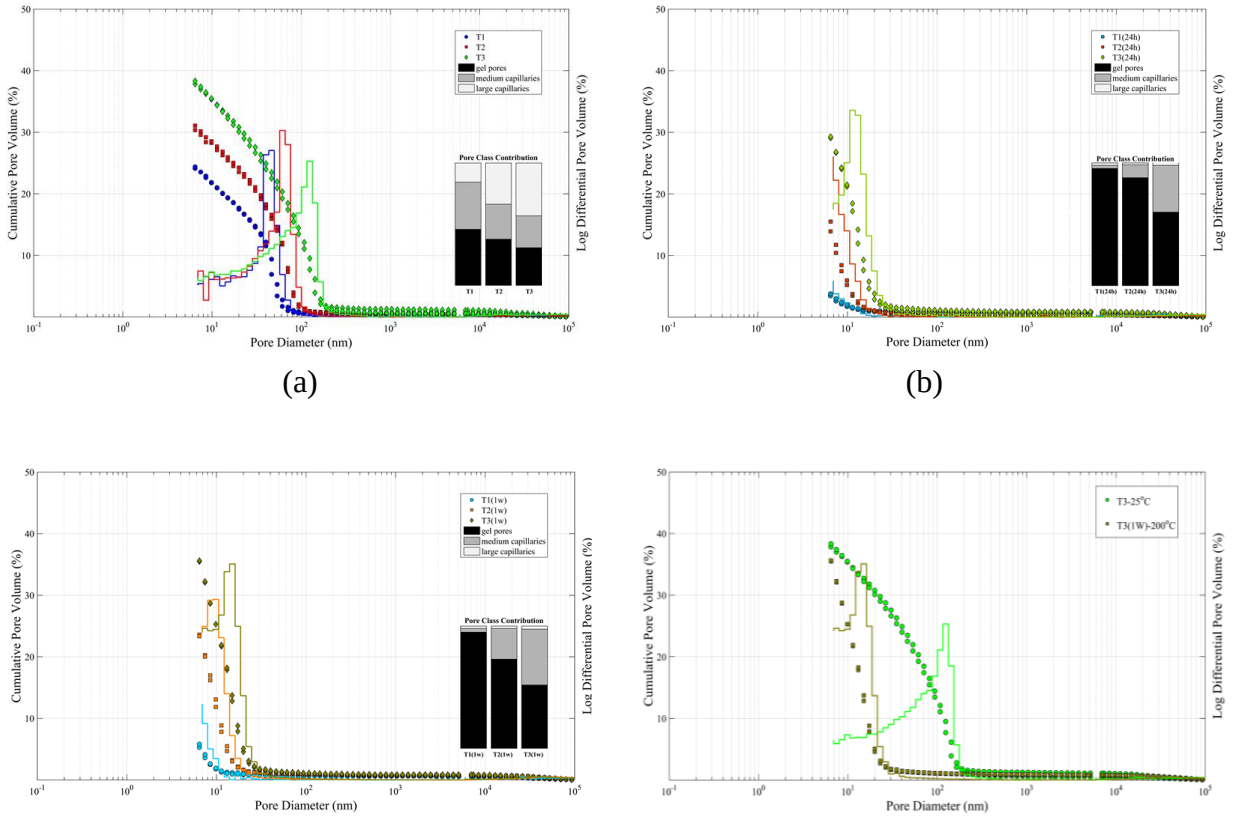

Figure 14. Evolution of pore size distribution with change in the solid volume fraction (SVF) and duration of hydrothermal curing of system T specimens. (a) Cured for 11 days at 25°C, (b) additional HTHP curing at 200°C and 21.1 MPa for 24 hours, (c) HTHP curing at 200°C and 21.1 MPa for 1 week, (d) a close look at the change in the pore structure of the specimen T3 (SVF=40%) after hydrothermal processing.

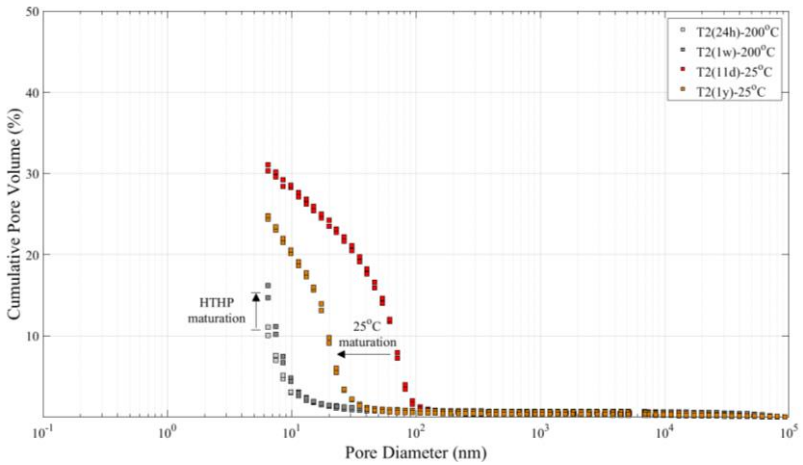

Figure 15. Enhanced mercury intrusion with prolonged hydrothermal processing of the mature cement system type T2

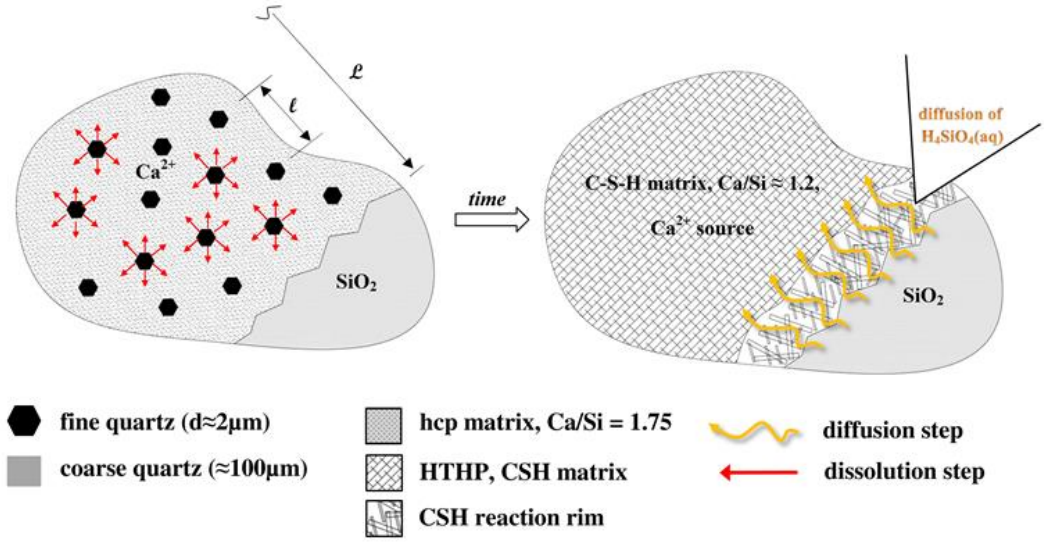

Figure 16. Schematic of the hypothesized microstructural changes in the silica-enriched cement system D1 with HTHP curing. Left: Prehydrated microstructure consisting primarily of hcp matrix with uniformly distributed fine quartz particles that act as a major local source of H_4SiO_4(aq) at the early stage of hydrothermal processing, and part of single coarse SiO_2 particle. Right: Final microstructure after HTHP curing. The fine SiO_2 has been completely consumed and the coarse silica particle has been activated to provide the additional SiO_2 required to lower the Ca/Si to the measured value of 0.84. A diffusion dominated process results in the formation of a boundary layer of CSH around the coarse particles.

TABLES

Table 1. Design and processing parameters of investigated cement systems with bimodal distribution of crystalline silica additive, specimens D1 and D2, and unimodal silica distribution in T-series.

	System				
	D1	D2	T1	T2	T3
SVF[1](%)	59		50	45	40
ρ_{sl} (kg/m^3)	2090		1972	1874	1777
silica[2] (%)	15/50	25/40		42 - fine	
w/c	0.61		0.54	0.66	0.81
w/s	0.24		0.34	0.42	0.51
$(Ca/Si)_{mix}$	0.38			0.83	
pre-curing	25°C for 7 days			25°C for 11 days	
HTHP curing	200°C, 20.7 MPa				

1 = Solid Volume Fraction, SVF = V_{solids} / V_{slurry} , where V_{solids} – volume of solid material including cement, V_{slurry} – volume of cement slurry, 2 = BVOB – by volume of the blend, α-quartz, fine silica/coarse silica

Table 2. Specific Surface Area (SSA) as determined from the SANS measurements.

	D1(1w)	D1(3m)	D1(6m)	D2(1w)	D2(3m)
C_P	49.96±2.4	50.4±2.6	41.7±2.2	95.7±2.9	103.7±2.9
SSA (m^2/cm^3)	62.7	63.2	53.5	120.1	130.1

* - C_P – Porod constant determined in the Q range 0.14-0.20 Å^{-1}

Table 3. Estimated elemental concentrations and sum of inorganic oxides (SOX) for the clusters of the calcium-silicate-hydrates group isolated in the statistical deconvolution analysis.

		Ca[a]	Si[a]	Al[a]	Fe[a,b]	S[a,b]	Mg[a,b]	SOX[c]
D1(1w)	#1	14.3±0.8	18.7±1.1	0.6±0.1	0.3±0.2	0.3±0.1	tr.	86±2
	#2A	15.2±0.4	17.9±0.5	0.5±0.1	0.2±0.1	0.4±0.1	tr.	85±2
	#3	15.1±0.6	16.7±1.1	1.0±0.3	0.8±0.4	0.5±0.1	0.3*	85±3
D1(3m)	#1	13.6±0.7	18.2±0.6	0.7±0.1	tr.	tr.	tr.	87±2
	#2A	14.6±0.4	17.1±0.8	0.7±0.2	0.3±0.2	0.3±0.1	tr.	85±2
	#2B	15.2±0.3	16.7±0.5	0.6±0.1	tr.	0.4±0.2	tr.	85±2
	#3	13.8±1.1	16.1±1.6	1.2±0.4	1.4±1.0	0.3±0.2	0.5±0.4	85±2
D2(1w)	#1	13.1±1.1	16.9±1.6	0.5±0.2	0.3±0.1	0.3±0.1	tr.	84±2
	#2A	14.0±0.4	16.1±0.6	0.4±0.1	tr.	0.3±0.1	tr.	83±1
	#3	13.4±0.8	14.7±0.9	1.3±0.4	0.9±0.4	0.3±0.2	0.3±0.2	82±2
D2(3m)	#2A	14.8±0.5	17.4±0.4	0.6±0.1	0.2±0.1	tr.	tr.	87±1
	#2B	14.8±0.4	16.7±0.5	0.8±0.2	0.5±0.2	0.2±0.1	tr.	86±1
	#3	14.0±0.7	16.2±1.2	1.1±0.4	1.1±0.7	0.3±0.1	0.4±0.3	86±2

a – atomic fraction in %, b – not used in the GMM fit as a classification variable, with an exception of D2(1w) sample, estimated as a mean from the clustered observations, c – as wt.%, tr. – traces, average value below 0.2 at.%

Table 4. Porosity, φ, bulk density, ρ_b, and specific gravity, ρ_{sk}, of systems D1 and D2 hydrothermally cured.

Sample		φ^*		$\rho_b^{*,\dagger}$		ρ_{sk}^*	
		25°C	200°C	25°C	200°C	25°C	200°C
D1	1w	na.	na.	1.83±0.01	na.	na.	na.
	3m		34.5±0.1		1.71±0.03 (1.71)		2.60±0.01
	6m		33.7±0.5		1.72±0.01 (1.70)		2.60±0.01
D2	1w	na.	33.1±0.5	1.85±0.02	1.75±0.01 (1.73)	na.	2.61±0.02
	3m		32.3±0.2		1.75±0.02 (1.72)		2.60±0.01

* - determined from overnight oven drying at 105°C, † - values in the parenthesis determined from MIP at 2 psi intrusion pressure, sample prepared by solvent exchange method followed by overnight oven drying at 55°C, na – not available

Table 5. Porosity, φ, bulk density, ρ_b, and specific gravity, ρ_{sk}, of system T cured for 24 h and 1 week.

Sample		φ^*		$\rho_b^{*,\dagger}$		ρ_{sk}^*	
		25°C	200°C	25°C	200°C	25°C	200°C
T1	24hr	40.3±0.2	40.4±0.4	1.61±0.01 (1.72)	1.58±0.01 (1.65)	2.69±0.01	2.66±0.01
	1w		39.6±0.3		1.61±0.01 (1.67)		2.67±0.01
T2	24hr	45.7±0.3	47.5±0.6	1.46±0.01 (1.55)	1.40±0.02 (1.47)	2.69±0.02	2.68±0.01
	1w		46.1±0.1		1.45±0.01 (1.49)		2.68±0.01
T3	24hr	51.5±0.2	53.1±0.1	1.28±0.01 (1.37)	1.25±0.01 (1.31)	2.65±0.01	2.66±0.01
	1w		52.8±0.4		1.27±0.01 (1.31)		2.68±0.01

* - determined from overnight oven drying at 105°C, † - values in the parenthesis determined from MIP at 2 psi intrusion pressure, sample prepared by solvent exchange method followed by overnight oven drying at 55°C

APPENDIX

Results of Profile Analysis of XRD Powder Spectra in the [25;34.5] range of 2θ

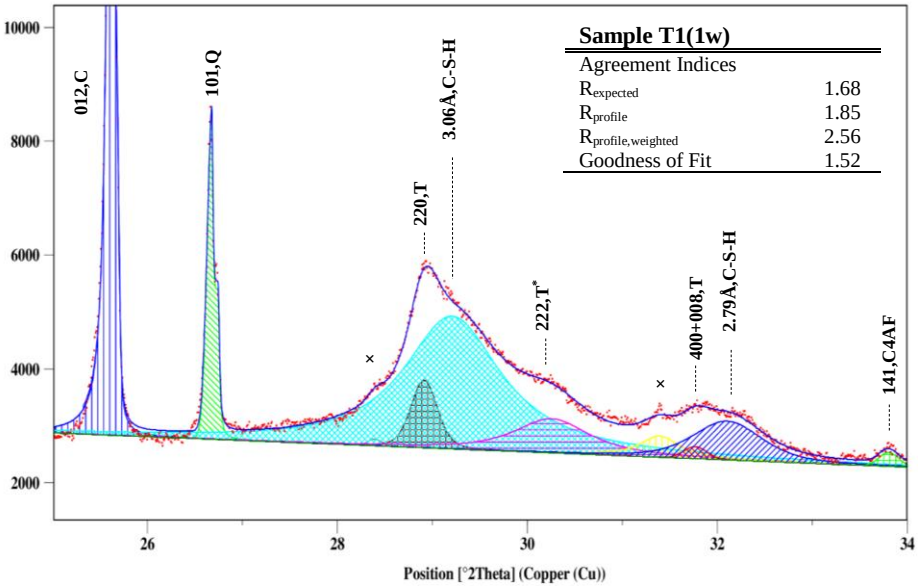

(a)

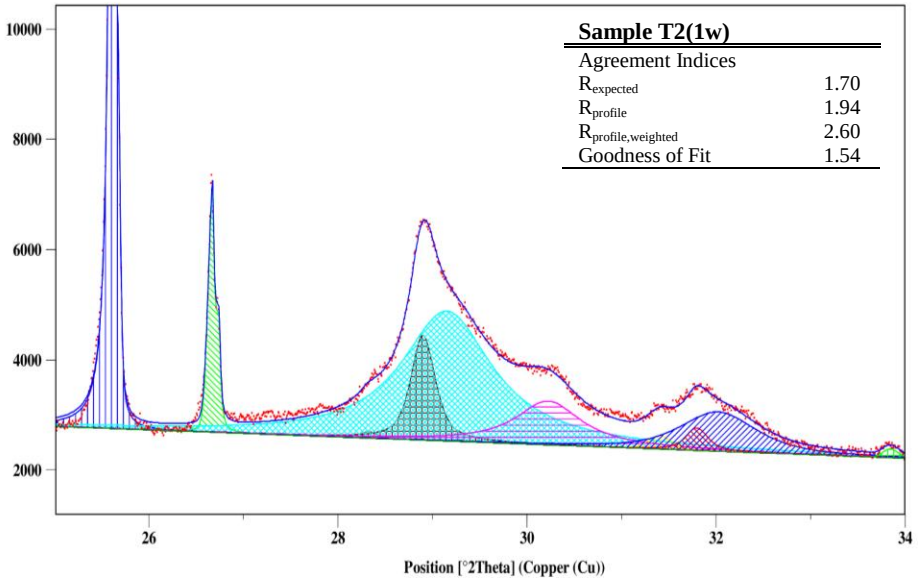

(b)

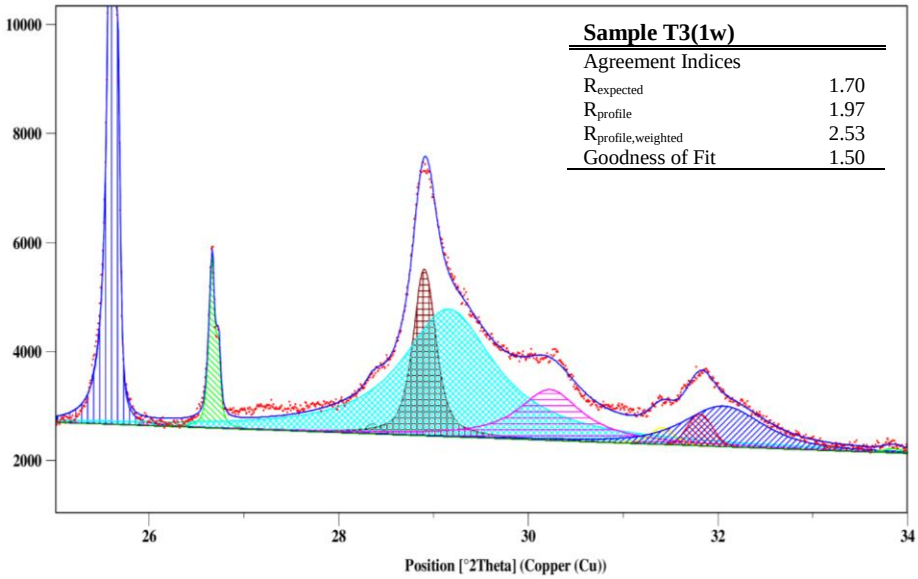

(b)

Figure A1. Results of the profile fitting applied to X-ray diffraction pattern collected on samples T-type cured for 1 week: (a) T1 with SVF = 50%, (b) T2 with SVF = 45%, and (c) T3 with SVF = 45%. Assumed notation: C – corundum, Q – α-quartz, T – 11Å tobermorite (diffraction peaks indexed after PDF 45-1480), C-S-H – diffraction line marked after [28, 31, 33], × – unidentified diffraction lines. Agreement indices expressed in %, $K\alpha_2$ lines not stripped.